JGR Solid Earth

RESEARCH ARTICLE
10.1029/2019JB018709

Shallow Megathrust Slip During Large Earthquakes That Have High *P* Coda Levels

Zhenbo Wu[1,2], Thorne Lay[2], and Lingling Ye[3]

[1]College of Geophysics, Chengdu University of Technology, Chengdu, China, [2]Earth and Planetary Sciences Department, University of California, Santa Cruz, CA, USA, [3]Guangdong Provincial Key Laboratory of Geodynamics and Geohazards, School of Earth Sciences and Engineering, Sun Yat-sen University, Guangzhou, China

Key Points:
- The estimated up-dip extent of slip during large megathrust earthquakes from finite-fault inversions often differs due to parameterization
- Modeling late *P* wave and early P_{coda} signals produced by deep water reverberations (*pwP*) improves late/triggered shallow slip resolution
- Several events with large P_{coda} levels are shown to have late shallow slip; deeper early aftershocks produce strong P_{coda} for other events

Supporting Information:
- Supporting Information S1
- Text S1
- Text S2
- Text S3
- Text S4
- Text S5
- Text S6
- Text S7

Correspondence to:
Z. Wu,
wuzhenbo@cdut.edu.cn

Citation:
Wu, Z., Lay, T., & Ye, L. (2020). Shallow megathrust slip during large earthquakes that have high *P* coda levels. *Journal of Geophysical Research: Solid Earth*, *124*, e2019JB018709. https://doi.org/10.1029/2019JB018709

Received 13 SEP 2019
Accepted 14 DEC 2019
Accepted article online 18 DEC 2019

Abstract Determining the up-dip extent of slip during large megathrust earthquakes is important for understanding tsunami generation, potential for subsequent failure of the shallow megathrust, and plate contact depth-varying frictional properties. Recent measurements of early P_{coda} amplitudes relative to direct *P* signals for the period range 7 to 15 s find high P_{coda}/P ratios for many events with finite-fault rupture models that have slip extending to near deep trenches, resulting in enhanced *pwP* (water-reverberation) generation. However, some events with high P_{coda}/P measures have finite-fault model solutions that vary in, or lack, shallow slip. We reexamine six large megathrust earthquakes with unexplained high P_{coda}/P ratios (30 July 1995 Chile, M_W 8.0; 17 November 2003 Aleutian, M_W 7.7; 12 November 1996 Peru, M_W 7.7; 7 October 2009 Vanuatu, M_W 7.6; 5 May 2015 Papua New Guinea, M_W 7.5; and 5 March 2002 Mindanao, M_W 7.5), inverting for slip models with depth-varying dip and varying bathymetry, adjusting kinematic parameters to better allow for the possibility of late shallow slip with associated strong *pwP* excitation. We confirm that modest patchy late shallow slip (~1 to 3 m) occurred near the trench for the 1995 and 2003 events, accounting for observed high P_{coda} levels and minor tsunamis. The 2009 event appears to have minor shallow slip, whereas the 1996, 2002, and 2015 events do not; their coda amplitudes are likely enhanced by early aftershocks. Refined modeling of the later stages of large megathrust ruptures, guided by P_{coda} levels, improves resolution of the up-dip limit of co-seismic slip.

1. Introduction

Most of Earth's largest earthquakes involve rupture of plate boundary megathrust faults in subduction zones (e.g., Allen & Hayes, 2017; Bilek & Lay, 2018; Kanamori, 2014; Lay, 2016; Lay et al., 2012). The seismogenic depth range of these shallowly dipping thrust faults typically extends from 12 ± 2-km to 45 ± 9-km depth (Hayes et al., 2018), although some events involve rupture that extends up to the seafloor near the trench (~2 to 8 km below sea level). When rupture occurs near the shallow toe of the overriding plate, usually in relatively low rigidity material, fault displacement can be atypically large and resulting seafloor deformation enhanced, resulting in strong tsunami excitation. If rupture does not extend to shallow depth in a large megathrust event, the shallow portion of the fault must accommodate the plate displacement either by aseismic slip or by occurrence of separate shallow ruptures. When isolated shallow ruptures occur, the low rigidity of the rocks above the megathrust produces low overall rupture velocity, weak radiated short-period energy, and, again, enhanced slip for a given seismic moment, with strong tsunami excitation (e.g., Lay & Bilek, 2007). These attributes are characteristic of a "tsunami-earthquake" (Kanamori, 1972). Establishing the up-dip limit of faulting in large megathrust ruptures is thus essential for understanding the strength of tsunami excitation, the potential for isolated tsunami-earthquakes to occur in the shallow portion of a subduction zone that either does or does not rupture in large deeper events, and the nature of depth-varying properties of the physical environment and/or intrinsic frictional variations along the megathrust.

Resolving the up-dip extent of rupture for large megathrust earthquakes is quite challenging. The subduction zone trench is far offshore, so regional on-land geodetic and seismic signals have limited resolution of the up-dip rupture, especially if deeper coseismic slip close to land dominates the rupture (e.g., Lay, 2018; Lay et al., 2012). Strong interference of direct down-going body waves with quickly following surface-reflected waves further limits the resolution of teleseismic signals. Low rupture velocities in the near-source environment at shallow depth can delay arrivals from shallow slip, producing a tapering tail in the event's moment-rate function for which typical simplified Green's functions and rupture model parameterizations may not

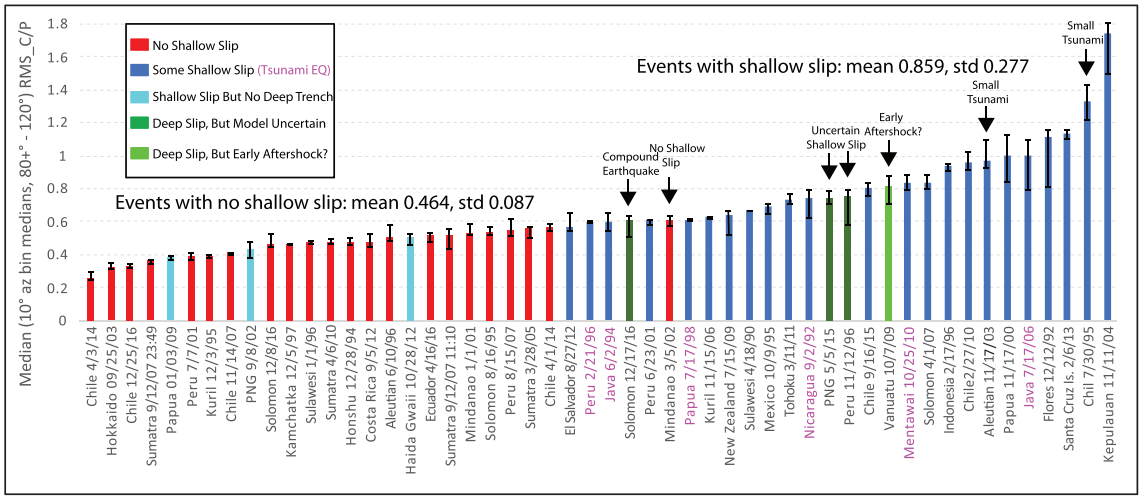

Figure 1. Event median *RMS_C/P*, for medians of 10° azimuthal bins of measurements at epicentral distances from 80 to 120°, ordered by increasing value for 52 large interplate thrust earthquakes (Lay et al., 2019). The range of the 40th and 60th percentile values is indicated by the bounds. The red bars indicate events that are thought to have no shallow slip based on the available slip models, while the blue bars are thought to have at least some shallow slip or only shallow slip. The cyan bars indicate events that rupture shallow depths but have no deep-water trench. The dark green bars have uncertain slip models but lack shallow slip in published results. The light green bar is for an event with an early aftershock possibly contaminating the coda. The magenta labels indicate tsunami earthquakes. The separate mean and standard deviation (*SD*) for the red and blue populations are shown above the distribution. The arrows highlight seven events with unexplained high coda levels that are discussed in the text.

provide good resolution. Thus, finite-fault inversions and moment-rate function deconvolutions for large ruptures often differ in the later stages of the source models (e.g., Bilek & Lay, 1999; Hayes, 2017; Meier et al., 2017; Vallée & Douet, 2016; Ye et al., 2016) due to their model parameterizations. Only recently have numerical methods advanced to allow accurate calculation of 3-D Green's functions in subduction zone structures including varying water depth (e.g., Qian et al., 2019; Wu et al., 2018) and such analyses are not yet routinely applied for constructing finite-fault models of large events. Rapid determination of the up-dip extent of faulting to assist in early tsunami warning by recognition of the potential enhancement in tsunami amplitude due to shallow slip thus remains a particularly difficult challenge.

A recently proposed approach to determining whether rupture reached shallow depths below a deep trench, with potential for rapid application for tsunami warning as well as to guide subsequent finite-fault modeling, exploits the tendency for slip under deep water to produce low frequency ringing in the *P* wave coda (P_{coda}; Lay & Rhode, 2019; Lay et al., 2019). This results from excitation of *pwP* signals, which involve acoustic reverberations in the water column generated by up-going *P* wave energy that reaches the seafloor above the slip zone. The multiple acoustic wave bounces within the water column shed *pwP* energy that is observed in the coda of the main teleseismic *P*+*pP*+*sP* wave packet, with a period that increases with the overlying water depth. Shallow rupture beneath a 6-km-deep trench will generate ~12-s period oscillations in the *P* coda; deeper rupture on the megathrust produces shorter-period, azimuthally varying *pwP* reverberations (Lay & Rhode, 2019). As a result, various ratios of P_{coda} amplitude relative to the main *P* wave amplitude provide simple measures that increase when slip extends to shallow depth.

Figure 1 shows event-median ratios of RMS P_{coda} amplitude to RMS *P* amplitude (*RMS_C/P*) for 52 large megathrust ruptures using global teleseismic vertical ground velocity recordings (Lay et al., 2019). Seismograms at epicentral distances of greater than 80 to 120° were filtered in the 7- to 15-s passband, median values of *RMS_C/P* measurements in 10° azimuthal bins were computed, and event-medians of the azimuthally binned data, along with 40 percentile and 60 percentile values, are plotted. Finite-fault models have been determined for all of these events from a variety of seismic, geodetic, and tsunami inversion and modeling efforts, and those models were used to classify whether the event had evidence of some shallow slip in a region with a deep trench, some shallow slip with no deep trench, no shallow slip, uncertain designation due to inconsistency among finite-fault models, or visible evidence of a large early aftershock contaminating the coda window. The duration of the *P* wave signals and the length of the subsequent

P_{coda} windows were guided by the duration of the moment-rate functions for each event and by minimizing overlap with other expected phases such as *PP*. Events with no evidence of shallow slip (red bars) tend to have relatively low P_{coda}/P ratios, while those with shallow slip in deep water environments (dark blue bars) have higher P_{coda}/P ratios. Events with shallow slip but lacking deep trenches (cyan bars) have low P_{coda}/P ratios in the 7- to 15-s passband. The quasi-bimodal distribution indicates the potential of using this simple parametric measurement to inform tsunami warning systems about the possibility of stronger than average tsunami having been generated for a large event due to the slip extending to shallow depth under deep water, or not.

While promising, it is important to understand the outliers in Figure 1; particularly the events with relatively high coda levels and ambiguous finite-fault model indications of shallow slip or no indications of shallow slip. It is also important to understand events with indication of shallow slip and particularly strong coda but relatively weak tsunami excitation. The arrows in Figure 1 highlight events of interest to understand better. The goal of the current study is to examine six of the corresponding outlying events, with four different characteristics: (1) events with very high coda and finite-fault models with some shallow slip, but low tsunami amplitudes (30 July 1995 Chile, 17 November 2003 Aleutian); (2) events with high coda and finite-fault models that have consistent deep slip but inconsistent shallow slip determinations (12 November 1996 Peru, 5 May 2015 PNG); (3) events with deep slip in their finite-fault models but some indication of an early aftershock contaminating the coda (7 October 2009 Vanuatu); and (4) the one true moderately high coda level outlier in the population which has two consistent finite-fault models lacking shallow slip (5 March 2002, Mindanao). The only additional ambiguous event flagged in Figure 1 is the 17 December 2016 Solomon Island event, but that earthquake is a compound event that appears to have initiated with an intermediate depth intraplate slab rupture that triggered megathrust faulting (e.g., Lay et al., 2017). Two of three published models for this event (U.S. Geological Survey-National Earthquake Information Center [USGS-NEIC]; Lee et al., 2018) indicate that the triggered megathrust slip extended to near the trench, but the shallow slip is small, the tsunami excitation is weak, and the rupture parameterization is complicated and rather ill-constrained, so further analysis is not likely to add decisive information for that event.

The spatial distribution and global centroid moment tensor (GCMT) best-double-couple solutions (https://www.globalcmt.org/CMTsearch.html) for the six events considered here are shown in Figure 2. They sample several different subduction zone environments, and none of these events generated huge tsunami (Lay et al., 2019). Their relatively high P_{coda}/P ratios apparent in Figure 1 require an explanation. This is important for two reasons. The first is to evaluate whether the basic P_{coda}/P measurement strategy intrinsically produces false alarms for early tsunami warning application, in the sense of high P_{coda} incorrectly indicating stronger tsunami than would be expected based on the mechanism, magnitude, and a typical rupture of the central megathrust depth range. If so, we want to evaluate whether there is a viable mitigation strategy to avoid false inference of shallow rupture. The second is to exploit the coda excitation to help develop improved finite-fault models for these events to reduce the ambiguity regarding occurrence of shallow slip: an important goal for evaluating depth-varying properties and potential for tsunami earthquakes in these regions.

The *RMS_C/P* ratios are simple measures of the event-characteristic level of P_{coda} versus *P*, so they are closely connected to the observed teleseismic waveforms. To evaluate the relatively high *RMS_C/P* ratios for the six events of interest, Figure 3 shows limited subsets of their broadband (band-pass filtered from 5 to 200 s) teleseismic vertical component ground displacement waveforms. We display 200-s duration time windows of the globally distributed data at epicentral distances of 60° to 100° to provide a feeling for the measurements in Figure 1. The red lines denote the time intervals used for measuring RMS amplitudes of *P* (between the first two lines) and P_{coda} (between the last two lines). Each waveform is normalized by its peak amplitude. The *PP* phase arrives after 150 s at 60° and moves-out in time relative to *P* with distance, as seen particularly clearly for the 2009 Vanuatu event (Figure 3d). Note the strong ~15-s period ringing in the coda windows for the 1995 Chile (Figure 3a) and 2003 Aleutian (Figure 3b) events, highlighted by the cyan boxes. The 1996 Peru event (Figure 3c) has some early strong arrivals in the coda (cyan) but lower later coda levels, which is reflected in the event median *RMS_C/P* in Figure 1. The 2009 Vanuatu (Figure 3d) and 2015 PNG (Figure 3e) events have coherent secondary arrivals that lack prolonged ringing. The 2002 Mindanao event (Figure 3f) has the lowest *RMS_C/P* measurement for the six events (Figure 1) but has very complex and incoherent coda signals, well above the background noise level. Extended profiles spanning the distance range 30 to 120°, and 500-s

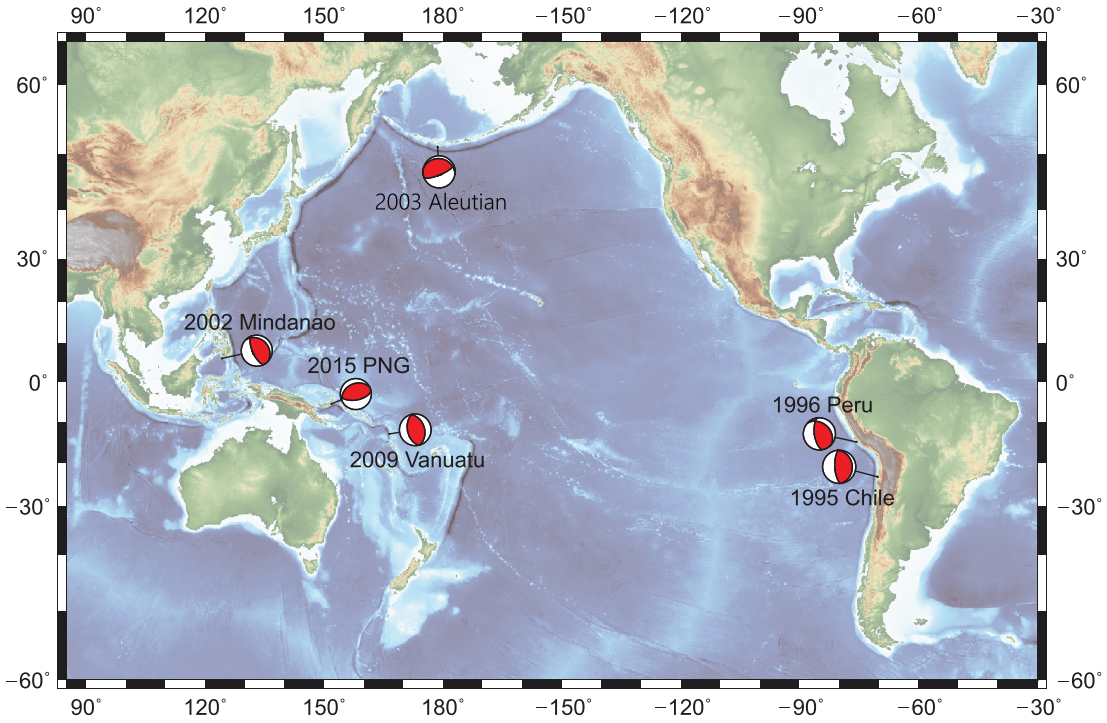

Figure 2. U.S. Geological Survey-National Earthquake Information Center (USGS-NEIC) epicenter locations and best-double-couple focal mechanisms from global centroid-moment tensor solutions for the six large subduction zone megathrust earthquakes considered here to understand why they have high *RMS_C/P* measures in Figure 1.

duration are shown for these events in Figures S1 to S6 in the supporting information for broadband and 7- to 15-s filtered displacements; the data correspond to the specific waveform populations measured in Lay et al. (2019).

In order to understand the causes of the enhanced coda levels for these six events, we perform updated finite-fault inversions using improved, although still approximate, Green's functions for varying oceanic bathymetry that accounts for first-order differences in *pwP* excitation as a function of slip placement relative to water depth. We seek to establish whether shallow slip occurred with strong *pwP* enhancement of the coda, and associated compatibility with the tsunami amplitudes. If not, is early aftershock activity during the coda window responsible for the *RMS_C/P* measurements? Resolving these issues will improve our understanding of these specific events and their up-dip limit of faulting. It will also address the outliers in the *RMS_C/P* measurements for the 52 large megathrust events in the database (Lay et al., 2019; Figure 1) that calibrate the strategy of using such measures in early tsunami warning applications.

2. Finite-Fault Inversion Method

We utilize a least-squares kinematic finite-fault inversion method applied to teleseismic *P* and *SH* wave ground displacements in the passband 0.005–0.9 Hz (200 to 1.1 s), seeking to improve the finite-fault rupture models for the six events in Figure 2 with relatively high *RMS_C/P* but uncertain shallow slip. The inversion procedure is basically that of Ye, Lay, et al. (2016), but we adapt the Green's functions and kinematic parameters to improve the modeling of early coda. The improvements mainly involve two structural features indicated in Figure 4. The first is the inclusion of varying ocean bathymetry in the source region crustal velocity structures when computing Green's functions (rather than a uniform 1-D structure). The varying water depth is extracted from ETOPO1 (https://www.ngdc.noaa.gov/mgg/global/) and accounts for first-order differences in *pwP* excitation for slip at different depths on the megathrust. The second improvement, increasingly used in finite-fault inversions, is to have depth-varying dip of the megathrust be specified using Slab2 (Hayes et al., 2018), rather than a single planar fault model.

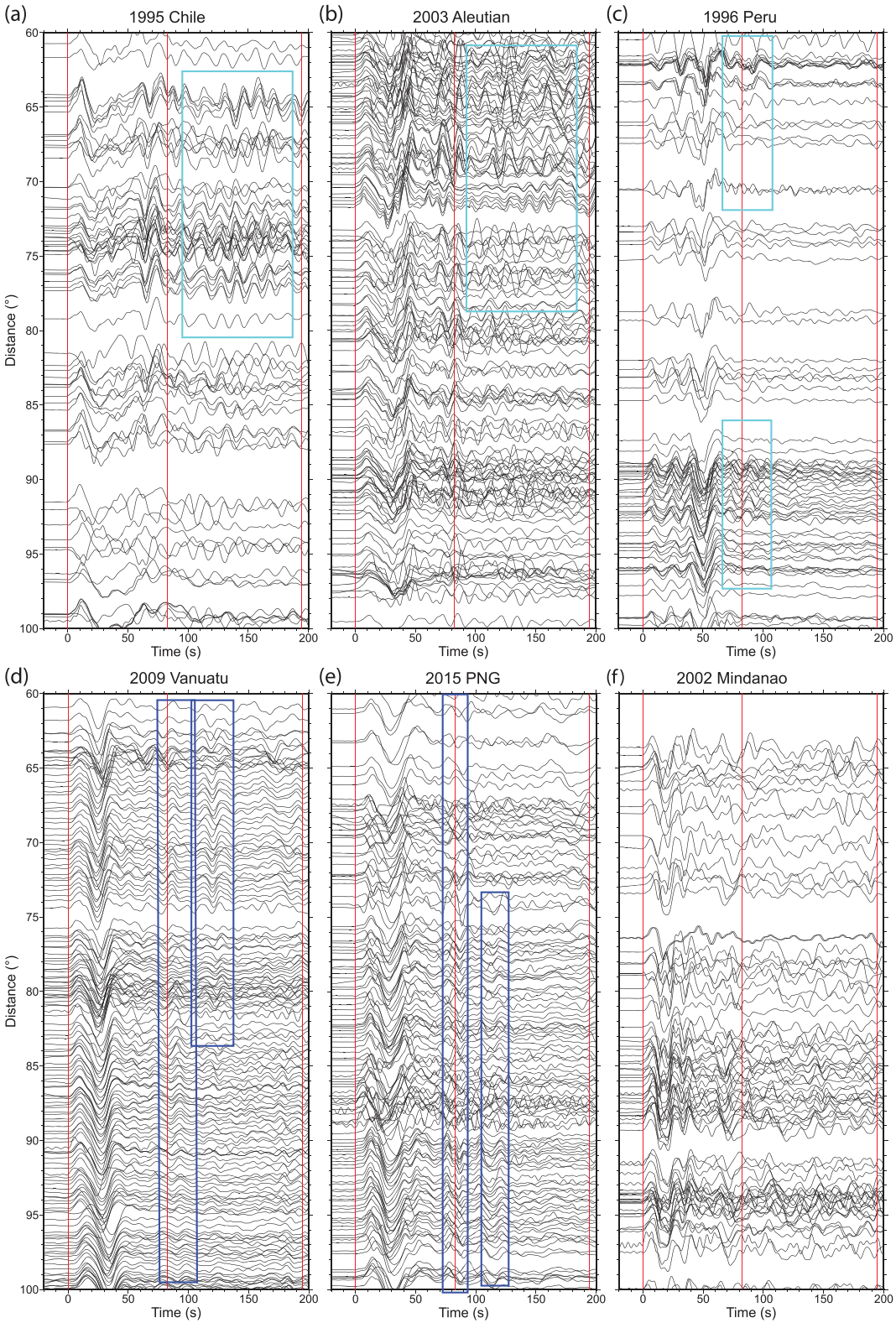

Figure 3. Broadband (band-pass filtered from 5 to 200 s) teleseismic vertical component ground displacement waveforms in the epicentral distance range 60 to 100° for the six events in Figure 2. Each waveform is normalized by its peak amplitude. For each profile, the first two red lines indicate the time interval for the *P* wave signal and the last two red lines indicate the P_{coda} window. The cyan boxes highlight the strong ~12- to 15-s period ringing in the coda windows for (a) 1995 Chile, (b) 2003 Aleutian, and (c) 1996 Peru events. The blue boxes display coherent discrete *P* arrivals after the direct *P*+*pP*+*sP* of the mainshock for (d) 2009 Vanuatu and (e) Papua New Guinea (PNG) events. The 2002 Mindanao event (f) has strong incoherent coda.

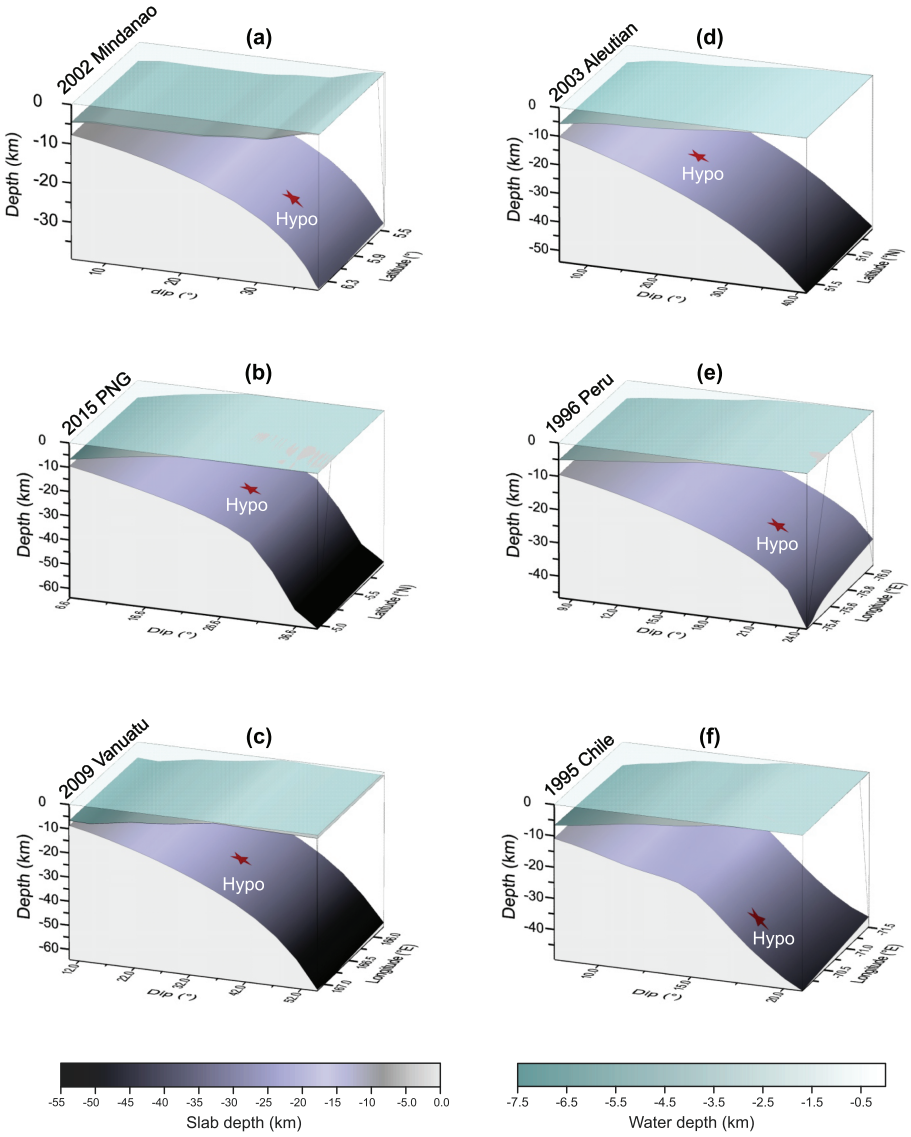

Figure 4. Subducting plate interface morphologies with depth-varying dip (model Slab2, Hayes et al., 2018) and varying oceanic bathymetry (ETOPO1) used to define quasi-2.5-D profiles for the finite-fault inversion for the six events in Figure 2 are displayed from (a) to (f). The red stars represent the hypocenter of each event, as adjusted to locate on the slab interface. The assumed fault plane for each event is parameterized by connected planar interfaces with depth-varying dip approximated from model Slab2.

We do not, however, compute Green's functions for fully 3-D structures (e.g., Qian et al., 2019; Wu et al., 2018), as that is a very expensive undertaking given the many subfaults involved in finite-fault inversions of large earthquakes and requires more detailed structural knowledge than typically available. Instead, we approximate the structure using 2.5-D calculations, assuming that the megathrust dip and ocean depth do not vary along the trench-parallel direction. Accordingly, we use single profiles through ETOPO1 and Slab2 that are representative for each source region. We adjust the hypocenter (often by several kilometers) to lie on the Slab2 interface at the USGS-NEIC epicentral location. The Green's functions are computed for segmented 1-D models with constant dip overlain by uniform water depth above each subfault in the rupture model. Essentially, the 3-D response is approximated by a stair-step sequence of overlapping 1-D models with varying water depth. Locally, *pP* and *sP* have steeply incident interactions with the low-velocity structure above each subfault, and this is reasonably represented for teleseismic ray parameters, as are the local

pwP reverberations in the overlying water column. However, this approach does not account in detail for 3-D path effects expected oblique to the trench. This approximate strategy allows us to fit many waveform features that are not matched in simple uniform 1-D models with constant water depth and constant fault dip across the entire model, but some features from 3-D path effects will not be fully accounted for by any quasi-2.5-D method. We have used this quasi-2.5-D approach successfully in several prior applications (e.g., Lay et al., 2016; Yamazaki et al., 2018; Ye, Kanamori, et al., 2016).

Our goal is to improve the fitting of the late interval of the source rupture and the generation of P_{coda} by using improved Green's functions in combination with adjusting the kinematic representation of the source. The models allow for continuous rupture to place slip at shallow depth on the fault, if the data inversion prefers that, or it allows for modest delays in shallow slip if a triggering process is involved. In order to provide the inversion with the opportunity to include shallow slip far offshore (with associated strong *pwP* excitation) during late stages of the rupture, we adjust kinematic parameters such as rupture velocity along-strike and along-dip, the subfault grid size, the subfault source time function parameterized by multiple overlapping triangles, and the time interval of the data inverted. For all events we use signal durations of 140 s from the onset of *P* or *SH* arrivals, significantly longer than the durations of coseismic slip. Typically, finite-fault inversions weight early portions of the waveforms more heavily, intrinsically, or by design, such that the late portion of the moment-rate function is not very reliable and the late ground motions are usually not well predicted. It is common to assume that the poor fit of late signals is due to inadequacy of the Green's function (e.g., Yagi & Fukahata, 2011) and model representation and to ignore any information in the early P_{coda}. However, here, our intent is to obtain finite-slip models for each event that are capable of explaining, rather than ignoring, observed late arrivals and early P_{coda}. Analysis of the quasi-2.5-D inversions for each event in Figure 2 and comparisons with previous findings are described in the next section.

3. Inversion Results

3.1. 1995 Chile

The 30 July 1995 M_w 8.0 Antofagasta, Chile, earthquake (Figure 5) initiated at 05:11:23.63 UTC (USGS-NEIC: https://earthquake.usgs.gov/earthquakes/) with epicenter 23.340°S, 70.294°W, and depth 45.6 km beneath Mejillones Peninsula, which protrudes trenchward to the west. The GCMT best-double-couple fault plane has strike, $\varphi = 354°$, dip, $\delta = 22°$, and rake, $\lambda = 87°$. Aftershocks from the USGS-NEIC catalog with magnitude $M_w \geq 4.5$ within the first month after the mainshock, along with GCMT best-double-couple focal mechanisms for $M_w \geq 5.0$ events, are shown in Figure 5, superimposed on the slip model obtained in this study. The trench in this region is quite deep (Figure 4f), varying from 7- to over 8-km deep.

Ihmlé and Madariaga (1996) first observed that the 1995 Chile earthquake has unusual strong monochromatic P_{coda} (Figures 3a and S1). They noted that band-limited signals often represent energy trapped by waveguides, such as crustal surface waves or acoustic *T*-waves in the oceanic SOFAR channel, and suggested that the late monochromatic waves are caused by spatially limited oscillations of the trench's water column. Despite this early study, various subsequent finite-fault inversions for the 1995 event have not sought to account for the observed strong coda level in the seismic data. The event generated a maximum tsunami water height of 3.0 m (National Oceanic and Atmospheric Administration [NOAA], https://www.ngdc.noaa.gov/hazard/tsu_db.shtml), but this has also not been systematically accounted for.

Ihmlé and Ruegg (1997) modeled the source rupture process using broadband surface waves and geodetic data. Their model indicates a heterogeneous slip distribution, with a major slip patch centered ~80 km south of the epicenter, with most slip located up-dip of the hypocenter. Several other published slip models for this event also indicate that the rupture extends unilaterally southward but does not reach the seafloor. Ruegg et al. (1996) modeled coseismic surface Global Positioning System (GPS) displacements and teleseismic body waves and suggested that whether the rupture reaches the trench depends on the fault dip used; for a dip of 24° slip does reach shallow depth. The GPS data used in this inversion have little resolution of far off-shore slip. Delouis et al. (1997) obtained a model with six subevents indicating that 80% of the body wave moment was released in the first 120 km of the rupture (40% near the hypocenter, 40% ~ 60 km to the south), and the rupture ended with a normal faulting subevent near the trench located about 130 km SSW of the epicenter. They do not show prediction of the early coda reverberations. Carlo et al. (1999) inferred a fairly smooth rupture with three embedded subevents, also finding that most of the slip occurred in the first 120 km or so.

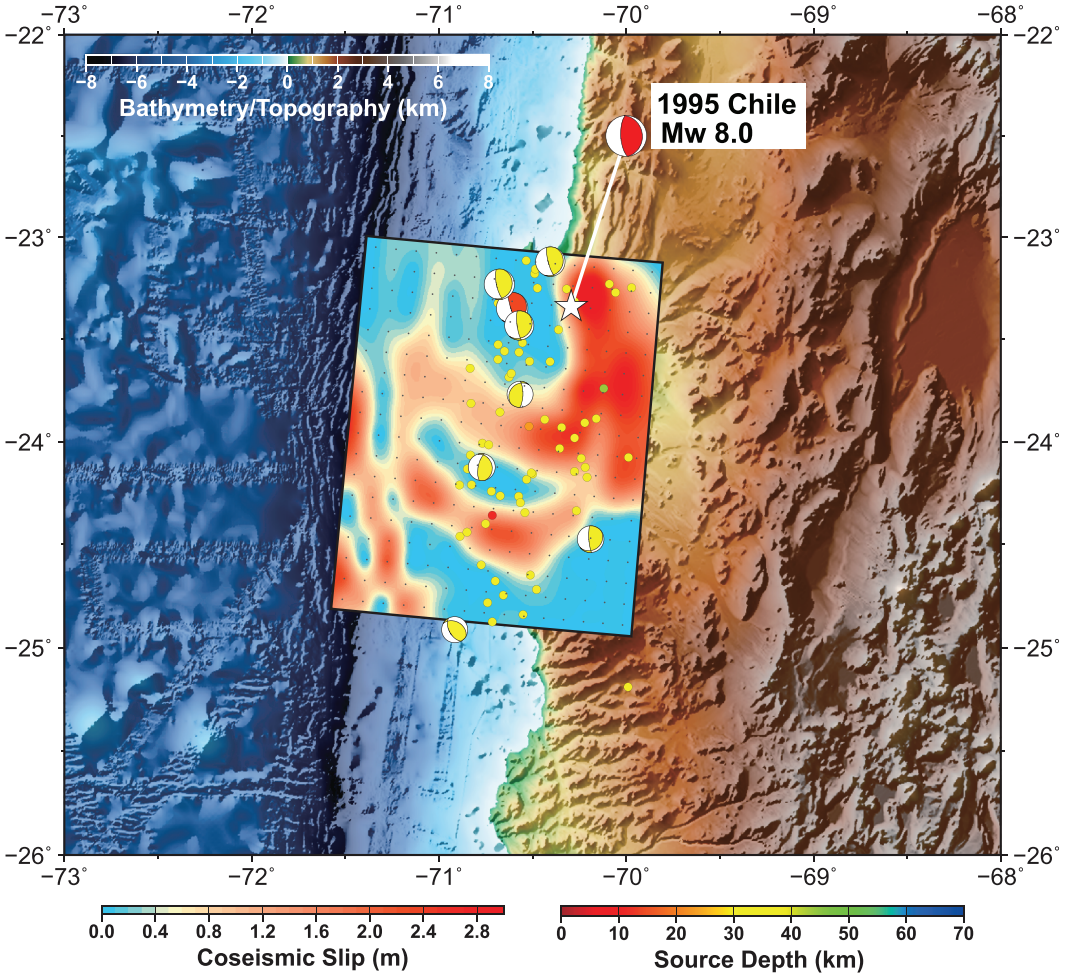

Figure 5. Surface projection of the finite-fault slip model for the 30 July 1995 M_w 8.0 Chile earthquake superimposed on regional bathymetry/topography. Aftershock locations ($M_w \geq 4.5$) within the first month are shown by circles color-coded for depth. Global centroid moment tensor (GCMT) solutions for the mainshock (linked to the epicenter at the white star) and for aftershocks with magnitude $M_w \geq 5.0$ are shown at their U.S. Geological Survey-National Earthquake Information Center (USGS-NEIC) epicenters.

Their model did not replicate the normal fault subevent near the trench inferred by Delouis et al. (1997), but they also could not fit the late *P* waves well with a thrust fault subevent. Klotz et al. (1999) use on-land GPS data, finding a model with most of the seismic moment released at less than 35 km in depth, with minor slip (~0.5 m) extending to the sea floor near the trench, but the off-shore resolution is very low. Another geodetic model, based on interferometric synthetic aperture radar and GPS data, also infers that most coseismic slip is up-dip of the hypocenter, possibly extending to near the trench in the south (Pritchard et al., 2002), but the model resolution of far offshore slip is shown to be very low. Slip models obtained from teleseismic *P* wave inversions by Ye, Lay, et al. (2016) using the same kinematic inversion routine used in this study, but assuming a single dipping fault plane and a uniform overlying water layer, indicate southward propagation with up-dip extent to depths of about 12 km. This guided Lay and Rhode (2019) to infer that some shallow slip did occur, but none of these models clearly account for the persistent ringing coda.

We expand the *P* wave data set of Ye, Lay, et al. (2016) and add *SH* wave observations to help separate fault slip from water reverberations, performing new kinematic inversions with quasi-2.5-D depth-varying dip and varying bathymetry. The 140-s-long data windows include several cycles of the early *P* coda. In our final model for the 1995 event (Figures 5 and 6), each subfault is a square with length and width of 11.25 km. The assumed rupture velocities along strike and dip are 2.75 and 2.25 km/s, respectively, favored after broad searches of both parameters. The subfault source time functions have four 2.5-s rise-time triangles shifted by

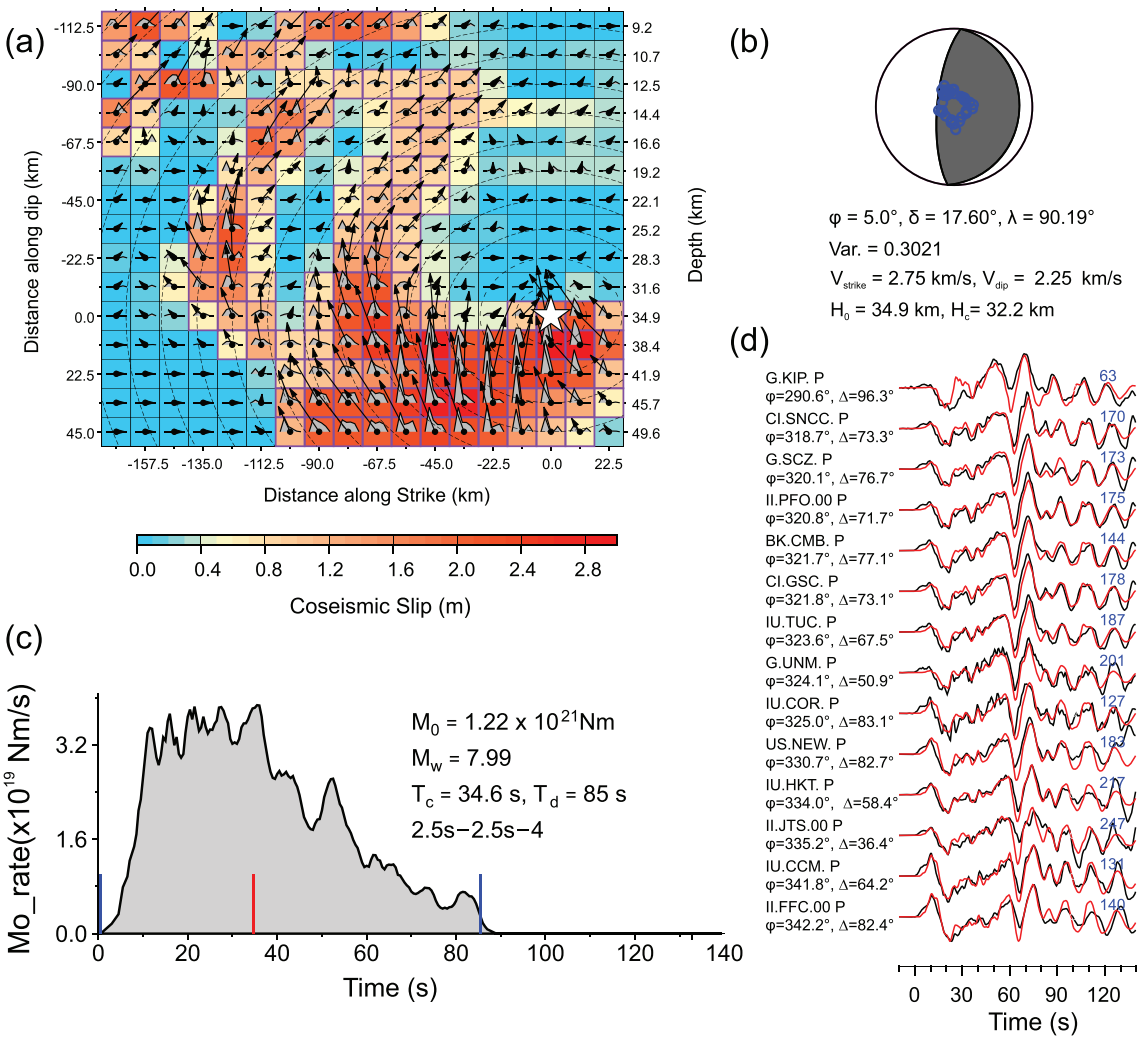

Figure 6. Finite-fault model for the 30 July 1995 M_w 8.0 Chile earthquake obtained using the quasi-2.5-D inversion. The fault plane dip varies from 7.6° at shallow depth to 21° at 50 km depth. (a) The slip distribution color-coded by slip amplitude. The subfaults outlined in purple have seismic moment ≥0.15 x maximum subfault moment. The white star represents the hypocenter. Arrows indicate the rake and relative slip amplitude for each subfault. The subfault source time functions are shown within each cell. The dashed circles indicate rupture front position in 5-s intervals. (b) The average focal mechanism with double couple strike (φ), dip (δ), and rake (λ). The blue circles indicate takeoff angles of *P* wave stations used in the inversion. (c) The moment-rate function. The blue ticks indicate the time span used to determine the total duration, T_d. The centroid time, T_c, is indicated by the red tick. (d) Comparisons of a subset of observed (black) and predicted (red) *P* waveforms. Below each station name the azimuth and epicentral distance relative to the source are indicated. The peak-to-peak amplitude of the data trace in microns is shown in blue. Each waveform is normalized to uniform amplitude. All waveform fits for this event are shown in Figure S7. A model with the shallowest four rows removed is shown in Figure S8.

2.5 s each, allowing total possible subfault duration of 12.5 s. The fault surface is assumed to be continuous with depth-varying dip ranging from 7.6° at shallow depth to 17.6° at the adjusted hypocenter depth (34.9 km) and 21° at 50-km depth (Figure 4f). The 5° strike is held fixed. Rake is allowed to vary by ±45° from a reference value of 90°. The maximum water depth above the shallowest subfaults is 7.5 km, which can generate ~15-s period *pwP* ringing if shallow slip occurs.

Figure 6a shows the slip distribution with color-coded slip amplitude and arrows indicating the variable rake. The early rupture extends slightly down-dip and southward followed by up-dip migration with patchy, late shallow slip of ~1–3 m near the trench. For the shallow subfaults, with upper edges 8.4 km below sea level, the overlying water depth is ~7.5-km deep (Figure 4f); thus, the Green's functions include strong ~15-s period *pwP* excitation, as expected. The combination of slip extending to ~85 s and the persistent *pwP* reverberations that are generated by shallow slip gives a good fit to the late oscillations in the 140-s-

long *P* signals (Figures 6d and S7). The average depth of slip is 32.2 km, and the centroid time of the moment-rate function is 34.6 s, comparable to the GCMT solution centroid depth of 28.7 km and centroid time of 33.4 s. The seismic moment is $M_0 = 1.22 \times 10^{21}$ Nm ($M_w = 8.0$).

The slip distribution shown in Figure 5 indicates that the rupture likely reaches to near the trench along an ~80-km-long stretch. The precise lateral extent and the spatial patchiness of the inverted slip are affected by the choice of kinematic parameters, but similar basic features are present in many models with varying parameters that we obtained. While the slip distribution is nonunique, if the model is truncated to have no subfaults shallower than 15-km depth, the fit to later coda reverberations is very poor, as seen in Figure S8. Our own standard procedure has typically been to distrust late slip on the edge of models, but in this case, the excellent waveform match to the coda gives us confidence that the shallow slip is not an artifact. Slip of up to 3 m near the trench can readily account for the 3-m maximum sea height observed for this event based on our modeling experience that shallow slip magnitude is roughly proportional to near-field peak tsunami amplitude (e.g., Lay et al., 2013; Li et al., 2016).

Previous studies (e.g., Carlo et al., 1999; Pritchard et al., 2002) suggested that there is no simple relationship between aftershocks and the slip distribution for this event and that the aftershock occurrence is likely related to stresses induced by postseismic rather than coseismic deformation. However, for our slip distribution, most aftershocks are located near the edges of coseismic large-slip regions (Figure 5), particularly the larger events that have focal mechanisms similar to the mainshock. This observation is consistent with the observation that regions of large-slip in mainshocks generally lack aftershocks (Beck & Christensen, 1991; Wetzler et al., 2018).

3.2. 2003 Aleutian

The 17 November 2003 M_w 7.7 Aleutian earthquake (06:43:06.8 UTC, epicenter 51.146°N, 178.650°E, depth 33.0 km; USGS-NEIC) struck near the eastern Rat Islands. The GCMT best-double-couple rupture plane is $\varphi = 280°$, $\delta = 19°$, and $\lambda = 122°$ (Figure 7). NEIC aftershocks with magnitude $M_w \geq 4.5$ and GCMT best-double-couple focal mechanisms for events with $M_w \geq 5.0$ within 1 month after the mainshock are distributed over a 150-km-long region (Figure 7).

The 2003 Aleutian event initiated near the hypocenter of the M_w 8.7 1965 Rat Island earthquake (Balakina & Moskvina, 2009; Beck & Christensen, 1991; Wu & Kanamori, 1973). For the 1965 earthquake, Beck and Christensen (1991) found three areas of large slip (interpreted as asperities) that correlate with laterally segmented blocks of the western Aleutian arc. They suggested that the 1965 mainshock initiated with failure of the eastern, largest asperity, which triggered sequential rupture of the segments to the west in a multiple asperity failure. The 2003 event appears to have reruptured within the region of the initial 1965 asperity.

The waveforms of the 2003 Aleutian event have high amplitude 7 to 15 s period P_{coda} (Figures 3b and S2), with sustained ringing at seaward azimuths and lower amplitudes at landward azimuths (Figures 8d and S9). The recorded tsunami in this remote area has a maximum water height of only 0.33 m (NOAA) so any shallow slip is likely to be relatively small. Because the stations at seaward directions have paths along radiation pattern nodes for down-going *P* waves (Figure 8b), we increase the weight of data traces at seaward azimuths in the finite-fault inversion to ensure that the inversion fits these waveforms to establish whether or not the ringing signals are generated by shallow slip with strong *pwP*. The other parameters in the finite-fault inversion are subfault length 16.5 km (along strike) and width 14.5 km (along dip), rupture velocity 2.0 km/s (along strike) and 1.5 km/s (along dip; selected from a broad search over widely ranging values), and subfault source time functions with five 3.5-s rise-time triangles shifted by 3.5 s each, giving total possible subfault durations of 21 s to provide enough time to fit the late *P* wave signals. The fault plane dip increases from 6.0° at shallow depth to 21.3° at the adjusted hypocentral depth of 22.7 km, to a dip of 34° at ~43-km depth (Figure 4d). The fault strike is 288° (slightly modified from the GCMT solution to fit the trench geometry), and the oblique reference rake is 122°. The maximum water depth above the shallowest subfaults is 6.1 km (Figure 4d), which will produce ~12-s period *pwP* ringing for any shallow slip.

Three published slip models for this event (Yagi, 2003; USGS-NEIC, Hayes, 2017; Ye, Lay, et al., 2016) show similar compact large-slip patches near the hypocenter. The models of the USGS-NEIC and Ye, Lay, et al. (2016) have minor (~1 m) slip near the trench in a localized region southwest of the hypocenter, and fit *P* wave ground motions for a duration of about 90 s, but predictions of later coda are not shown. The

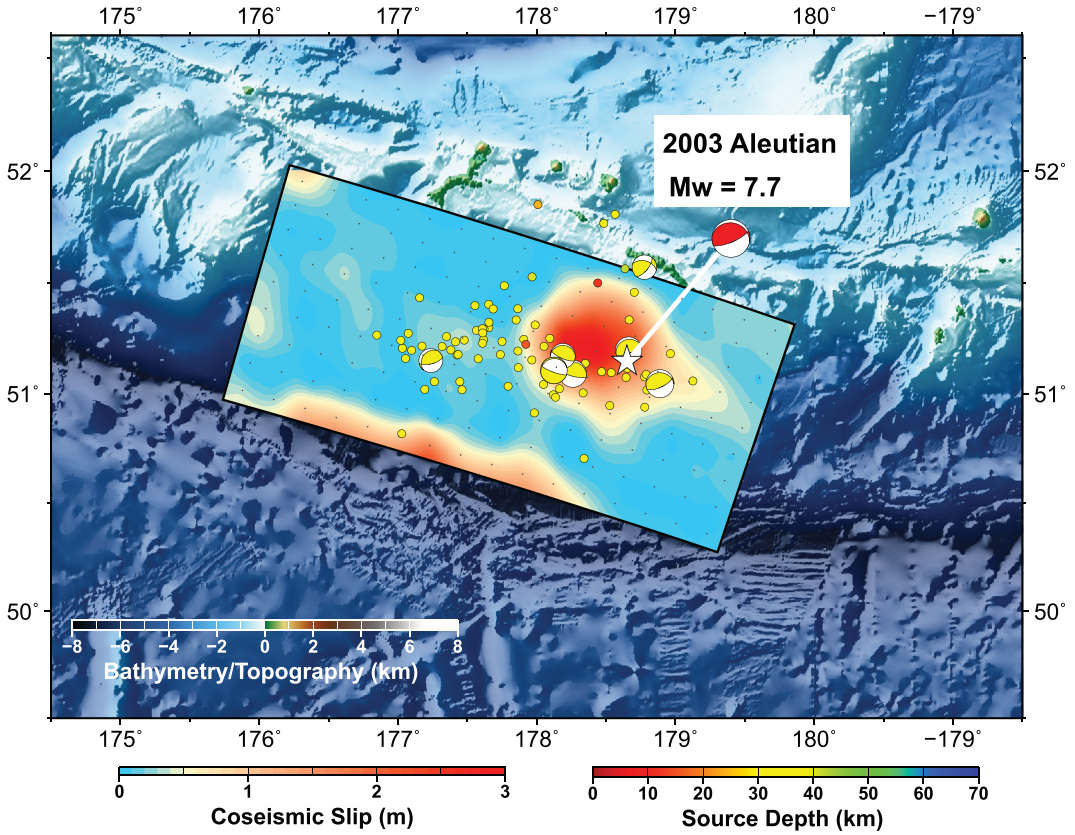

Figure 7. Surface projection of the finite-fault slip model for the 17 November 2003 M_w 7.7 Aleutian earthquake superimposed on regional bathymetry/topography. Aftershocks ($M_w \geq 4.5$) within the first month are shown by depth-colored circles. Global centroid moment tensor (GCMT) solutions for the mainshock (linked to the epicenter at the white star) and for aftershocks with magnitude $M_w \geq 5.0$ are shown at their U.S. Geological Survey-National Earthquake Information Center (USGS-NEIC) epicenters.

moment-rate functions of the two models show 1 to 2 discrete late pulses from 40–60 s and 60–80 s. Such later pulses are usually not given much credence as being part of the source process, but in this case, there are clearly *P* wave motions that lead to the late pulses. These features prompted Lay and Rhode (2019) to label this event as likely having some slip at shallow depth, but that designation was not with high confidence.

As shown in Figures 7 and 8a, our favored updated slip model for the 2003 Aleutian earthquake also has a relatively compact ~50-km by 50-km large-slip patch centered northwest of the hypocenter, and the corresponding interval of the moment-rate function has a triangular pulse with ~35-s duration (Figure 8c). This is followed by ~4 secondary pulses extending to ~108.5 s, which are associated with narrow strip of very shallow slip of up to 2 m. The spatial placement of the shallow slip is not well resolved, given the nonuniqueness of the model kinematics, but shallow slip is preferred over deeper slip for the late subevents. The shallow slip under deep water generates long-period *pwP* phases, particularly for the seaward stations that have weak direct *P* energy, and this likely contributes to the strong oscillations in the later part of the *P* signals well (Figures 8d and S9). The last pulse in the data window is not well modeled, and there could either be additional shallow slip events at later time or perhaps the *pwP* predictions are underestimated and require fully 3-D Green's functions to account for their prolonged nature. If the rows in the slip model at depths less than 14 km are removed, the inversion achieves only slightly degraded fits to the early coda (Figure S10), because it gives a sequence of slip pulses to match the data, as the *pwP* from these deeper slip events is not strong. But the peculiar periodicity of the required slip events strongly indicates that the data are better explained as being produced by a combination of shallow slip with water multiples rather than exclusively as deeper late slip events. Thus, we infer that late rupture with shallow slip under deep water does appear to be responsible for the high P_{coda}/P measure for this event (Figure 1).

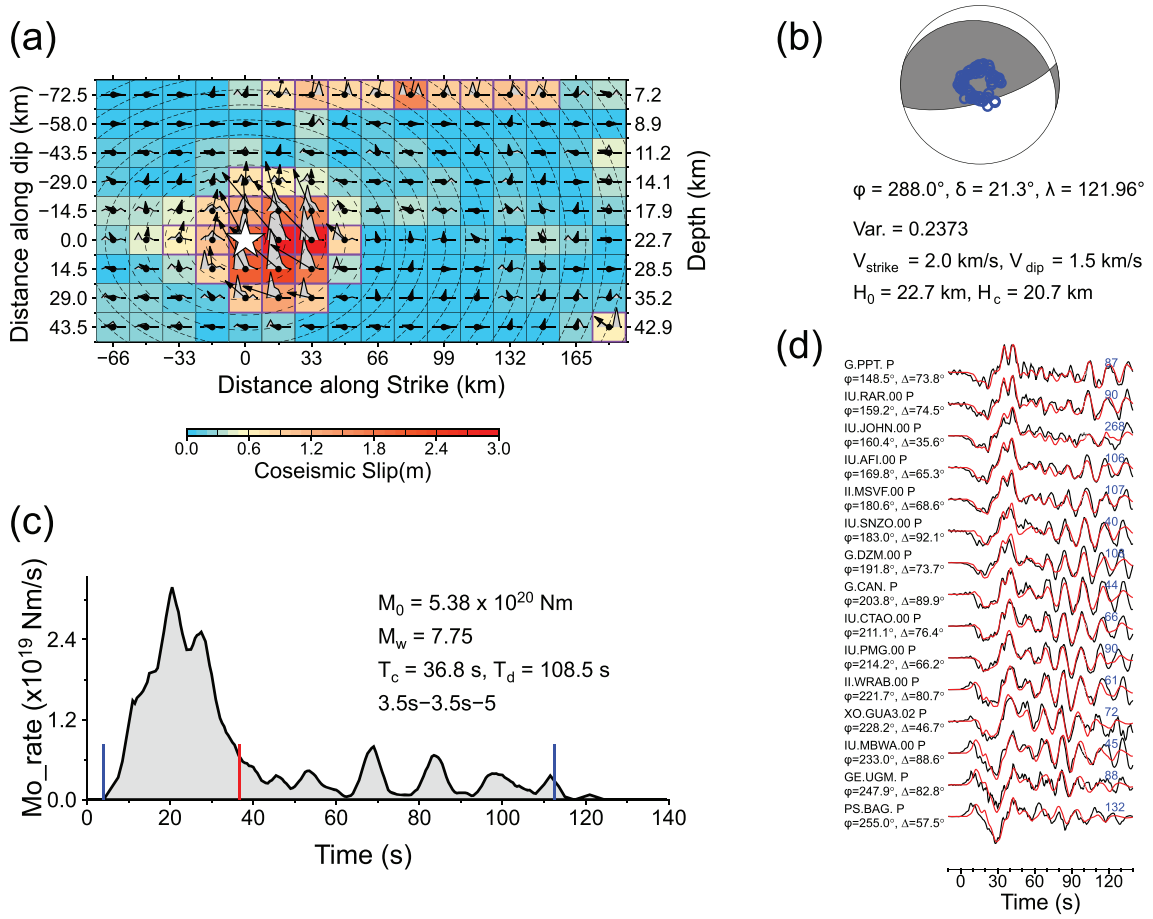

Figure 8. Finite-fault model for the 17 November 2003 M_w 7.7 Aleutian earthquake obtained using the quasi-2.5-D inversion. The fault plane dip varies from 6.0° at shallow depth to 41° at about 54 km depth. All panels follow the format of Figure 6. (a) The slip distribution with color-coded slip amplitude. (b) The average focal mechanism and *P* wave data distribution. (c) The moment-rate function. (d) A subset of comparisons of observed (black) and predicted (red) *P* waveforms. All waveform fits for this event are shown in Figure S9. A model with the shallowest three rows removed is shown in Figure S10.

The coseismic large-slip region of the 2003 Aleutian event is fringed by large aftershocks, and there are very few aftershocks at shallow depth where the discrete late slip patch is located (Figure 7). The aftershocks extend west of the large-slip zone. Since the shallow slip is <2 m, the observed weak tsunami is accounted for; the large coda reflects the high efficiency of excitation of *pwP* by even modest shallow slip. This emphasizes that when using P_{coda} levels to infer shallow slip, the overall event size, which is moderate in this case, should still be considered as the first-order indicator of tsunamigenesis with occurrence of shallow slip likely enhancing the size of the tsunami (Lay et al., 2019).

3.3. 2009 Vanuatu

On 7 October 2009, the northern portion of the Vanuatu subduction zone ruptured in three major shallow thrust earthquakes within 70 min (e.g., Cleveland et al., 2014). The first event (22:03:14.47 UTC, 13.006°S, 166.510°E, depth 45.0 km; USGS-NEIC) had M_W 7.6 and was followed 15 min later by a larger event (M_W 7.8) ~50 km to the NNW. A third event, with M_W 7.4, struck about 1 hr later adjacent to the southern end of the first event. We consider only the first event, for which the GCMT focal mechanism (Figure 9) corresponds to underthrusting with best-double-couple nodal plane $\varphi = 344°$, $\delta = 41°$, and $\lambda = 87°$. Aftershocks encompassing the triplet sequence with $M_w \geq 4.5$ and GCMT focal mechanisms for $M_w \geq 5.0$ events within the first month are shown at their NEIC epicenters in Figure 9. The aftershock seismicity for this sequence with three large events is naturally more intense and distributed than for the Chile and Aleutian mainshocks. The temporal and spatial clustering of activity indicates that a broad region was close to failure, with effective triggering occurring, raising the probability of an early aftershock having occurred soon after the first event.

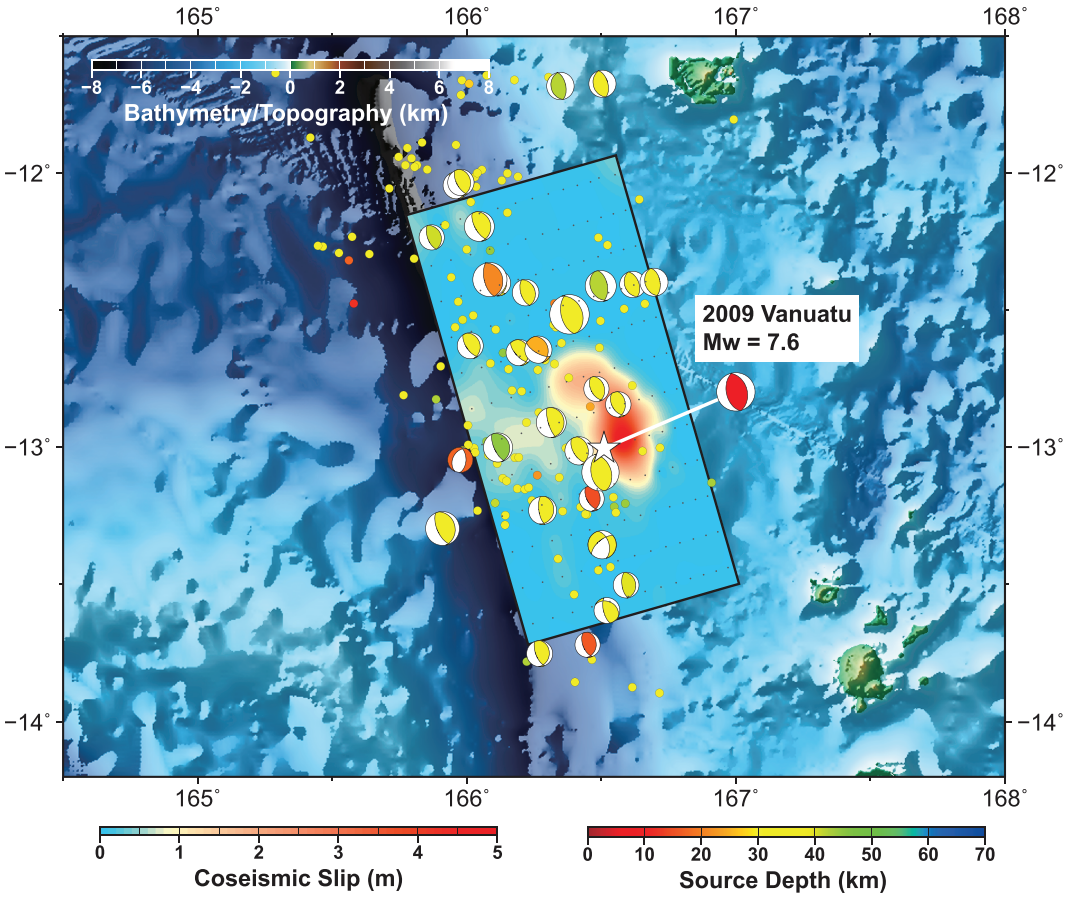

Figure 9. Surface projection of the finite-fault slip model for the 7 October 2009 M_w 7.6 Vanuatu earthquake superimposed on regional bathymetry/topography. Aftershocks ($M_w \geq 4.5$) within the first month are shown by depth-colored circles. Global centroid moment tensor (GCMT) solutions for the mainshock (linked to the epicenter at the white star) and for aftershocks with magnitude $M_w \geq 5.0$ are shown at their U.S. Geological Survey-National Earthquake Information Center (USGS-NEIC) epicenters.

In our finite-fault inversion for the Vanuatu event, the subfault size is 15.0 km along strike and 8.5 km along dip, and the final selected rupture velocities are 2.15 km/s along strike and 1.15 km/s along dip. The subfault source time functions are parameterized by four 3.5-s rise-time triangles shifted by 3.5 s with total possible subfault rupture durations of 17.5 s. The fault plane has varying dip of 10.2° at 8.4-km depth, 35.5° at the adjusted hypocentral depth of 27.3 km, and 54.8° at 64-km depth. The strike (344°) and reference rake (87°) are from the GCMT solution. The maximum water depth near the trench is about 7.3 km (Figure 4c), which favors long-period (~15 s) ringing of *pwP* generated by any shallow slip in the first row of the model.

The moment-rate function for our finite-fault model (Figure 10c) has a triangular source pulse duration of ~30 s followed by several much smaller subevents, with an overall centroid time of 20.2 s. The slip model has a relatively compact large-slip region extending from 22- to 44-km deep, as shown in Figures 9 and 10a. Additional minor slip (<1 m) extends up-dip from the hypocenter to shallow depth near the deep-water trench accounting for the secondary subevents. The overall event size, with or without minor shallow slip can account for the <0.3-m maximum tsunami water height reported for this event (NOAA), although there is potential for confusion in run-up reports with the larger event 15 min later. The *P* (+*pP*+*sP*) waves and associated *pwP* ringing slip account for the ground motions from onset to ~80 s quite well (Figures 10d and S11), but later coherent discrete arrivals from 80 to 140 s (Figure 3d) are not accounted for, even by models with further extended fault dimensions, longer subfault durations, and lower rupture velocities. The high ground motion amplitudes from 80 to 140 s are thus not readily attributed to late shallow slip with strong *pwP*, so an alternate explanation is needed. Additionally, three previously published slip models for this event

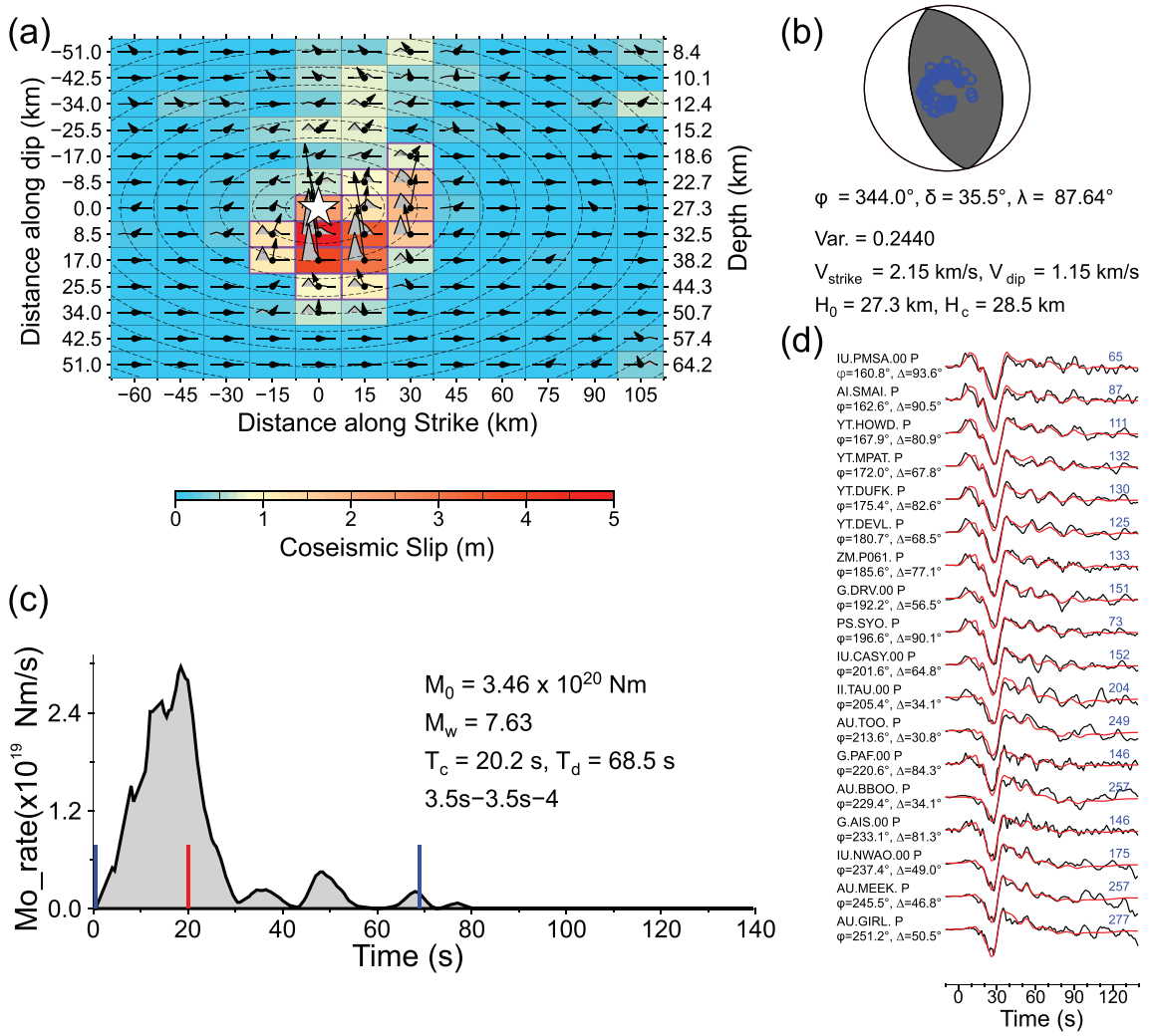

Figure 10. Finite-fault model for the 7 October 2009 M_w 7.6 Vanuatu earthquake obtained using the quasi-2.5-D inversion. The fault plane dip varies from 10.2° at shallow depth to 54° at about 64 km. All panels follow the format of Figure 6. (a) The slip distribution with color-coded slip amplitude. (b) The average focal mechanism and *P* wave data distribution. (c) The moment-rate function. (d) A subset of comparisons of observed (black) and predicted (red) *P* waveforms. All waveform fits for this event are shown in Figure S11.

consistently show a compact large-slip patch similar to the main feature in our model without any evidence for strong shallow rupture reaching to the seafloor (Cleveland et al., 2014; Hayes, 2017; Ye, Lay, et al., 2016). The large-slip zone and the up-dip small-slip patch are largely devoid of aftershocks but are bracketed by the large M_W 7.8 and 7.4 events to the northwest and southeast, respectively (Figure 9).

Our interpretation is that the later arrivals and high coda levels evident in the distance profiles (Figures 3d and S3) are body waves generated by early aftershocks at around 80 and 110 s after the mainshock that contaminate the putative coda interval of the mainshock, giving rise to a high RMS_P_{coda}/P measure. These are not readily accounted for by a very prolonged finite-fault model so they may differ in mechanism. We sought to confirm these as discrete events by high pass filtering the seismograms, but the overall coda levels are too high to isolate early aftershocks. Indeed, the high 7- to 15-s coda levels persist for hundreds of seconds for this event (Figure S3). The *SH* waves are not very well fit for this event, especially in the signal after 60 s (Figure S11), suggesting that the structure may be more complicated than the model we used for the slip inversion or that multiple early aftershock mechanisms do differ from the mainshock. While we find that there is a shallow small-slip region up-dip of the main slip patch for this event, the slip is not strong

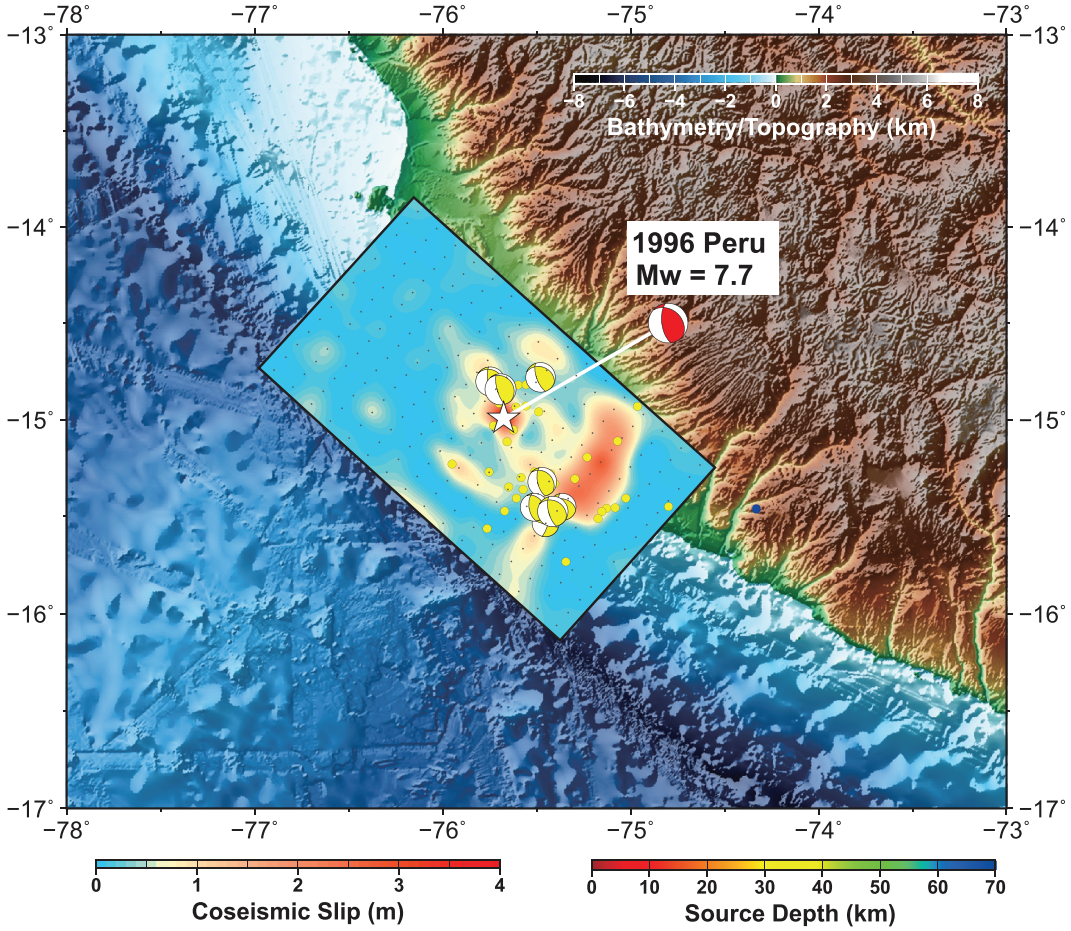

Figure 11. Surface projection of the finite-fault slip model for the 12 November 1996 M_w 7.7 Peru earthquake superimposed on regional bathymetry/topography. Aftershocks ($M_w \geq 4.5$) within the first month are shown by depth-colored circles. Global centroid moment tensor (GCMT) solutions for the mainshock (linked to the epicenter at the white star) and for aftershocks with magnitude $M_w \geq 5.0$ are shown at their U.S. Geological Survey-National Earthquake Information Center (USGS-NEIC) epicenters. Slip in the shallowest rows is not well resolved.

enough to produce persistent *pwP* reverberations extending long into the P_{coda}. However, the clear evidence of early discrete impulsive ground motions, which are likely due to early aftershocks in the distance profiles (Figure 3d), accounts for the high P_{coad}/P measure (Figure 1), as speculated by Lay and Rhode (2019). Recognizing the presence of impulsive arrivals without strong *pwP* ringing by inspecting seismogram profiles like Figure 3d would easily prevent a false alarm regarding possibility of enhanced tsunami.

3.4. 1996 Peru

The 12 November 1996, M_w 7.7, Peru, earthquake (16:59:44.03 UTC, 14.993°S, 75.675°W, depth 33.0 km; USGS-NEIC) occurred along the subduction interface between the Nazca ridge and the South American plate (Figure 11). Buoyancy of the underthrusting ridge causes the trench to be relatively shallow along the rupture zone (<5 km; Figure 4), and it is deepest to the southeast, on the ridge flank. The GCMT best-double-couple focal mechanism has a rupture plane with $\varphi = 312°$, $\delta = 33°$, and $\lambda = 55°$. The aftershock seismicity with $M_W \geq 4.5$ is relatively sparse for an earthquake of this size (Figure 11).

Prior investigations of the coseismic slip for the 1996 Peru event have not resolved the presence of any shallow slip near the trench. The USGS-NEIC model (Hayes, 2017) uses a steep constant fault dip of 33° and does not extend to the trench. It shows a band of large slip beneath the coast extending unilaterally southeastward. The slip inversion of Ye, Lay, et al. (2016) with 33° dip also has a large-slip region located southeast of the hypocenter, with some patchy shallow slip near the upper boundary of their fault model, which again does

not reach to the trench. Spence et al. (1999) also presented a model with constant 33° dip, with slip extending unusually deep, to 66 km, whereas Swenson and Beck (1999) placed the primary slip at about the same distance along strike but at shallower depth below the coastline. Joint inversion of broadband teleseismic and interferometric synthetic aperture radar data locates a main asperity 50 km southeast of the hypocenter between 20- and 40-km depth (Salichon et al., 2003), similar to the USGS-NEIC inversion. While these previous studies did not resolve any near-trench shallow slip, they were not well parameterized to explore that possibility. The event has a moderately high value of *RMS_C/P* (Figure 1), and there are some large amplitude signals early in the P_{coda} window from 60 to 120 s after the onset of *P* (Figures 3c and S4). Overall, the coda levels are lower and have significantly less monochromatic ringing than the 1995 Chile and 2003 Aleutian events and there are no clear isolated secondary arrivals like those for the 2009 Vanuatu event (Figure 3).

We set up our model to allow the possibility of imaging any shallow slip. For our finite-fault inversion for the 1996 Peru event, the subfault dimensions are 14.5 km along strike and 10.0 km along dip, with the rupture velocities being 2.0 km/s along strike and 1.75 km/s along dip. The subfault source time functions are parameterized by four 3.5-s rise-time triangles shifted by 3.5 s with total possible subfault durations of 17.5 s. The fault plane has variable dip from 8.1° at 8.9-km depth to 20.6° at the adjusted hypocentral depth of 26.2 km and 24.2° at ~50-km depth. Slab2 dips are consistently lower than 33° used in prior inversions. The strike of 312° and reference rake of 55° are from the GCMT solution. The water depth in the source structure above the subfaults closest to the trench is 4.3 km, which shortens the period of any *pwP* reverberations produced by shallow slip to be less than 9 s. As noted above, the water depth deepens to the southeast to about 5 km, so some paths toward that azimuth could have longer period *pwP*, but our 2.5-D modeling will fail to account for this.

Although the fault grid extends bilaterally relative to the hypocenter, our inversion result shows predominantly unilateral southeastward rupture with very little slip to the northwest of the hypocenter. A large-slip region locates 30 to 80 km southeast of the hypocenter and extends about 70 km along dip (Figure 12a), with patchy slip (<1.5 m) extending up-dip to the trench, as well as locating up-dip and down-dip near the hypocenter. The minor off-shore slip could contribute to the observed tsunami water height of only 0.4 m (NOAA). The waveform fits shown in Figures 12d and S12 display good prediction of moderate ringing after the direct *P* waves for up to ~90 s. With the moment-rate function tapering off after ~ 60 s, some of this energy (highlighted in the cyan box in the distance profile in Figure 3c) could involve short-period *pwP* from the shallow slip under moderately deep water. However, truncating the model to have no subfaults shallower than 15-km deep does not prevent the inversion from fitting the data almost as well by enhancing slip just up-dip of the hypocenter (Figure S13). We consider the evidence for any shallow slip for this event to be marginal, although there are some secondary pulses in the coda that might be fit better with a fully 3-D calculation. The moment-rate function in Figure 12c is more jagged than those for the 1995 Chile, 2003 Aleutian, and 2009 Vanuatu events, corresponding to the more complex megathrust slip distribution. Aftershocks again tend to locate near the margins of large-slip regions, with relatively little activity at shallow depth (Figure 11). There is a notable cluster of larger aftershocks in the gap between the main large-slip zone and the shallow weak-slip patches. Overall, the slip model for this event does not provide a compelling case for shallow slip near the moderately deep-water trench that could account for the relatively high P_{coda}/P measure, but we do not fully account for later pulses that might be due to 3-D scattering effects or early aftershocks.

3.5. 2015 Papua New Guinea

A large earthquake doublet occurred near East New Britain, Papua New Guinea, on 29 March 2015 and 5 May 2015 (Heidarzadeh et al., 2015) with both events having $M_w = 7.5$. We focus on the second event (01:44:06.38 UTC, 5.462°S, 151.875°E, depth 55.0 km; USGS-NEIC), because available slip models for the 29 March 2015 event are consistent in not indicating shallow slip (USGS-NEIC; Heidarzadeh et al., 2015; Ye, Lay, et al., 2016). The GCMT best-double-couple focal mechanism for the 5 May 2015 event has a thrust plane with $\varphi = 245°$, $\delta = 33°$, and $\lambda = 77°$ (Figure 13). Aftershocks with $M_W \geq 4.5$ from the USGS-NEIC catalog and $M_w \geq 5.0$ events with GCMT focal mechanisms within 1 month after the mainshock indicate significant shallow megathrust earthquake activity (Figure 13), unlike for the other events discussed here. Several additional aftershocks are distributed landward of the hypocenter, some at depths greater than 40 km. There is high earthquake activity and numerous instances of triggering interactions between large events in this region (e.g., Lay et al., 2017; Lay & Kanamori, 1980). The observed tsunami was smaller

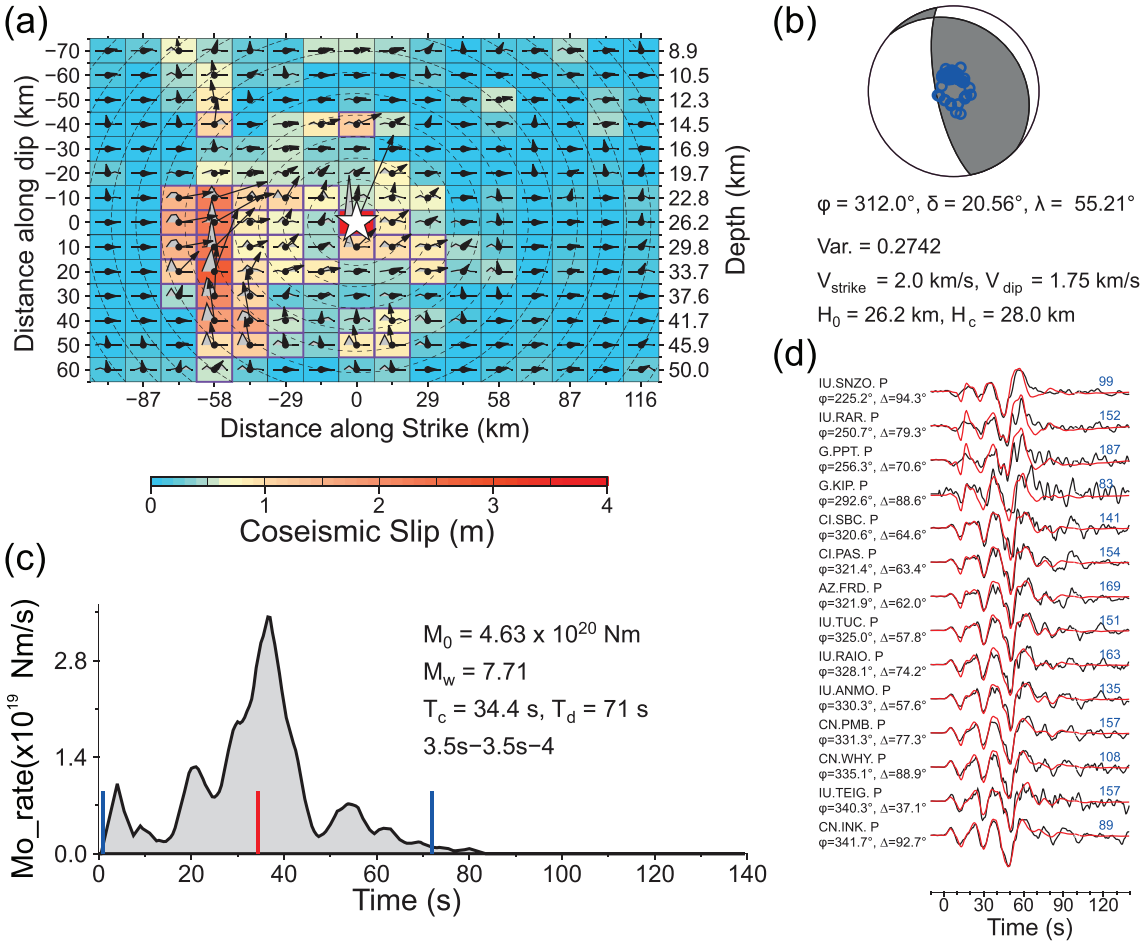

Figure 12. Finite-fault model for the 12 November 1996 M_w 7.7 Peru earthquake obtained using the quasi-2.5D inversion. The fault plane dip varies from 8.1° at shallow depth to 24.2° at about 50 km depth. All panels follow the format of Figure 6. (a) The slip distribution with color-coded slip amplitude. (b) The average focal mechanism and *P* wave data distribution. (c) The moment-rate function. (d) A subset of comparisons of observed (black) and predicted (red) *P* waveforms. All waveform fits for this event are shown in Figure S12. A model with the shallowest four rows removed is shown in Figure S13.

than that of the 29 March event located ~100 km to the northeast, and the tsunami signal is clear at only one tide gauge station, with a wave height of ~0.6 cm (Heidarzadeh et al., 2015); NOAA reports a maximum water height of 1 m for this event.

There have been several prior studies of this earthquake. The USGS-NEIC rupture model has a compact slip region in the depth range 20 to 50 km extending 60 km northeast along strike from the hypocenter. Heidarzadeh et al. (2015) use teleseismic data to determine a slip model with the rupture velocity being constrained by tsunami waveform fitting. They find a source area of 100 km × 80 km, centered ~ 15 km east of the epicenter beneath New Britain with slip of up to 0.5 m. These two studies do not indicate any shallow slip near the trench. Ye, Lay, et al. (2016) obtained a slip model with two discrete slip patches, one similar to those in the two studies noted above and another narrow patch at very shallow depth on the megathrust. The latter study fit teleseismic *P* waveforms for an 80-s time window using a single fault plane with fixed strike and dip and a source velocity model with no water layer. This model intrinsically cannot generate any *pwP*, so the occurrence of the shallow slip patch is uncertain, as is its ability to match the moderately high coda level for this event (Figures 1, 3e, and S5). The distance profile in Figure 3e shows discrete pulses in the time interval 70 to 130 s after the arrival of direct *P* (highlighted by blue boxes), that increase the coda amplitude leading to the moderately high P_{coda}/P ratio measure.

We obtain a slip model with depth-varying dip and varying bathymetry. The trench in this region is deep (Figure 4b), and the water depth above the shallowest row in the model is 7.2 km. The subfault size is

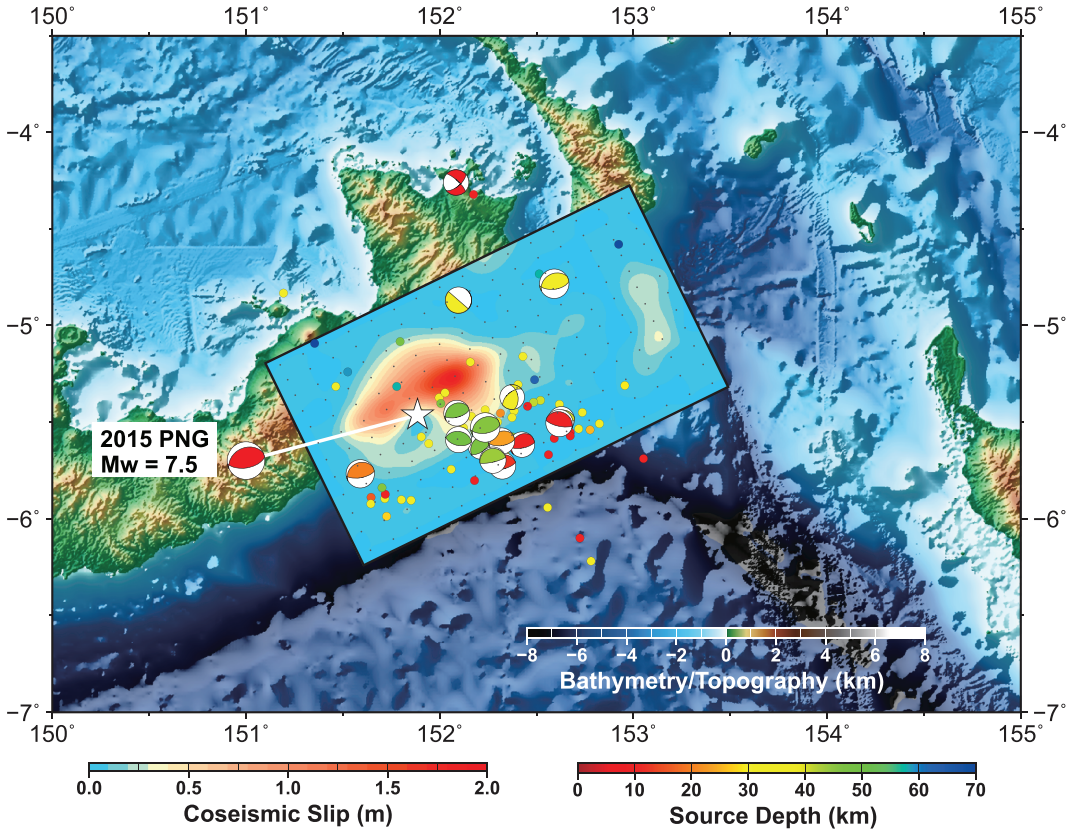

Figure 13. Surface projection of the finite-fault slip model for the 5 May 2015 M_w 7.5 Papua New Guinea earthquake superimposed on regional bathymetry/topography. Aftershocks ($M_w \geq 4.5$) within the first month are shown by depth-colored circles. Global centroid moment tensor (GCMT) solutions for the mainshock (linked to the epicenter at the white star) and for aftershocks with magnitude $M_w \geq 5.0$ are shown at their U.S. Geological Survey-National Earthquake Information Center (USGS-NEIC) epicenters.

14.5 km along strike and 12.0 km along dip, and the final rupture velocities are 2.0 km/s along strike and 1.0 km/s along dip. The subfault source time functions are parameterized by 3 3.5-s rise-time triangles shifted by 3.5 s each with total possible subfault duration of 14 s. The fault plane dip is 6.5° at 9.3-km depth, 25.9° at our adjusted hypocentral depth of 24.6 km, and 39.4° at 63-km deep. The strike (244°) and reference rake (75°) are slightly modified from the GCMT solution.

The resulting slip model is shown in Figures 13 and 14a. The rupture initially spreads down dip and along strike near the hypocenter, reaching 50-km depth and extending ~60 km northeastward. This main slip patch is similar to that in prior models. There is an ~37-s duration triangular pulse in the moment-rate function associated with rupture of this patch (Figure 14c). No slip is imaged at shallow depth, in contrast to the model of Ye, Lay, et al. (2016), even though the slow rupture velocity along dip provides a long time interval for any shallow slip to have been placed there. As there is no long-period ringing in the waveforms, the inversion does not activate slip in the shallowest rows of the model where strong *pwP* could be generated. The moment-rate function instead shows a moderate isolated pulse around 75 to 90 s after the onset. This corresponds to an isolated slip patch with <0.5-m slip amplitude about 145 km northeast of the hypocenter. This is beyond the rupture zone of the preceding 29 March 2015 event (USGS-NEIC; Heidarzadeh et al., 2015; Ye, Lay, et al., 2016), suggesting that remote slip was dynamically triggered by the 5 May 2015 event. This feature matches a clear arrival in the data with systematic azimuthal variation in timing from 70 to 90 s after the *P* wave onset (Figures 14d and S14) and corresponds to the arrival highlighted by the first blue box in Figure 3e. The model does not account for an even later arrival observed from 100 to 120 s, but the azimuthal moveout of that signal (Figure 14d) indicates a similar along-strike location for the corresponding slip. These secondary pulses do not generate strong *pwP* coda, so they appear to originate from the central depth range of

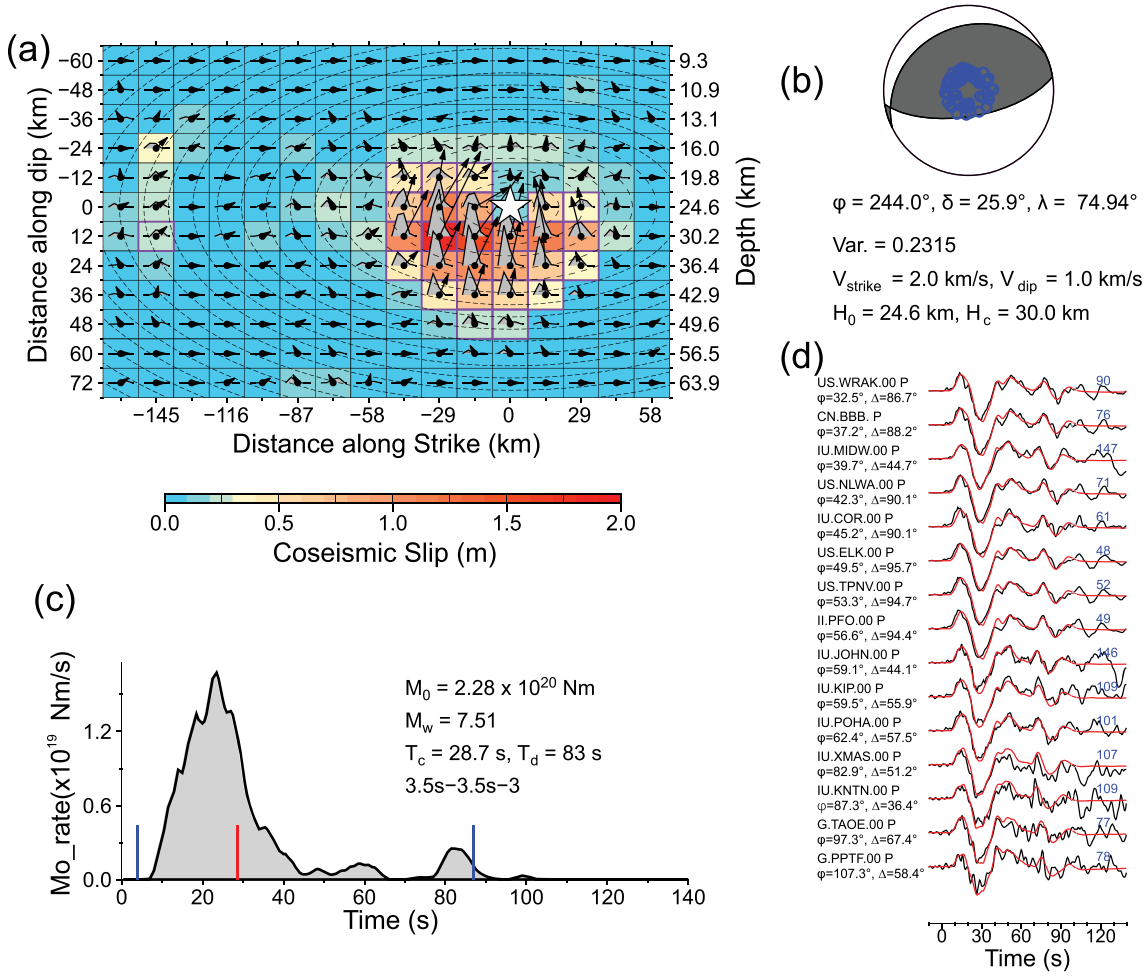

Figure 14. Finite-fault model for the 5 May 2015 M_w 7.5 Papua New Guinea earthquake obtained using the quasi-2.5-D inversion. The fault plane dip varies from 6.5° at shallow depth to 39.4° at about 63 km. All panels follow the format of Figure 6. (a) The slip distribution with color-coded slip amplitude. (b) The average focal mechanism and *P* wave data distribution. (c) The moment-rate function. (d) A subset of comparisons of observed (black) and predicted (red) *P* waveforms. All waveform fits for this event are shown in Figure S14.

the megathrust. Based on the aftershock locations in Figure 13, one might have anticipated some shallow coseismic slip, but this does not appear to be the case; rather the thrust-faulting aftershocks again fringe the large-slip region. They do not reliably guide assessment of shallow slip, unlike the situations when there is extensive outer rise normal faulting seaward of shallow slip (Sladen & Trevisan, 2018; Wetzler et al., 2017).

This source region experienced a previous earthquake (17 November 2000, M_w 7.8) in the same epicentral area as the 5 May 2015 event, with shallower GCMT centroid depth (17.0 km versus 38.3 km for the 2000 and 2015 events, respectively). The 17 November 2000 event has high *RMS_C/P* value (Figure 1) and was designated as an event with some shallow slip based on the finite-fault inversions from Ye, Lay, et al. (2016) and the USGS-NEIC model, both of which have significant slip at shallow depth. This directly contrasts with our model for the 5 May 2015 event; plausibly, the 2000 event released any strain accumulation in the shallow megathrust and too little time had passed for it to rebuild to a triggerable level. Several other inversions proposed slip concentrated just down-dip of the hypocenter for the 17 November 2000 rupture (Yagi & Kikuchi, 2000) or northeast of the epicenter (Park & Mori, 2007) without slip near the trench, but their parameterizations were not designed to allow for the possibility of shallow slip. The 17 November 2000 event was actually one of two large aftershocks of an M_W 8.0 strike-slip event along New Ireland the day before, with another thrust event on 16 November 2000 (M_W 7.8; e.g., Geist & Parsons, 2005) located

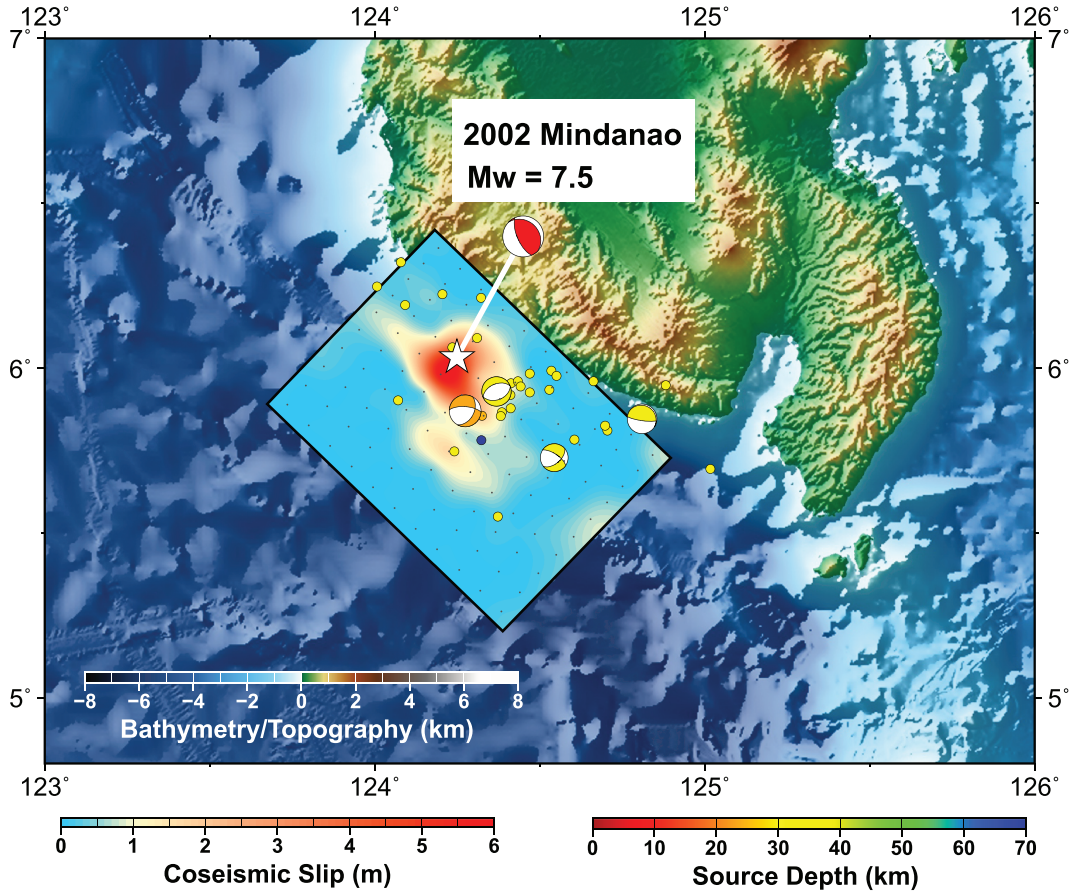

Figure 15. Surface projection of the finite-fault slip model for the 5 March 2002 M_w 7.5 Mindanao earthquake superimposed on regional bathymetry/topography. Aftershocks ($M_w \geq 4.5$) within the first month are shown by depth-colored circles. Global centroid moment tensor (GCMT) solutions for the mainshock (linked to the epicenter at the white star) and for aftershocks with magnitude $M_w \geq 5.0$ are shown at their U.S. Geological Survey-National Earthquake Information Center (USGS-NEIC) epicenters.

near the secondary triggered event in our model for the 5 May 2015 event. Analyses of past earthquakes in this complex region suggest that efficient triggering occurrences are controlled by persistent asperity patches, regional high earthquake productivity, and contortion of the subducting Solomon Sea plate (Geist & Parsons, 2005; Lay & Kanamori, 1980), which drapes around the corner between the northeasterly subduction beneath Bougainville and the northwesterly subduction beneath New Britain (Cooper & Taylor, 1989).

3.6. 2002 Mindanao

The 5 March 2002 Mindanao earthquake (21:16:09.13 UTC 6.033°N, 124.249°E, depth 31.0 km; USGS-NEIC) ruptured offshore of southern Mindanao in a somewhat ill-defined subduction zone (Figure 15). It generated a 3-m maximum water height (NOAA). The event occurred near the two largest twentieth century Philippine earthquakes: the 1918 Celebes Sea earthquake (M_w 8.3) and the 1976 Moro Gulf earthquake (M_w 8.0). Both of those prior events triggered large tsunami and caused widespread damage. Stewart and Cohn (1979) suggested that the 1976 earthquake represented the first seismic evidence for a northeast-dipping subduction zone beneath Mindanao in the Moro Gulf, North Celebes Sea. They observed significant variation in the mechanism of mainshocks and their largest aftershocks in this region. Beck and Ruff (1985) further studied the rupture process of the 1976 event, finding that it had a very rough moment-rate function.

The GCMT best-double-couple solution for the 5 March 2002 earthquake has seismic moment 1.94×10^{20} Nm (M_w 7.5), with thrust fault orientation $\varphi = 314°$, $\delta = 25°$, and $\lambda = 70°$. Figure 15 shows NEIC

aftershocks ($M_W \geq 4.5$) and GCMT focal mechanisms ($M_w \geq 5.0$) within 1 month after the mainshock. As had been observed for the prior events, the larger aftershock focal mechanisms differ from the mainshock thrust geometry, indicating that they are intraplate events. If early aftershocks occurred with such distinct faulting geometry, the body wave radiation patterns should have produced complex ground motions that will not be well modeled by slip on the megathrust.

Our finite-fault inversion for the 2002 event has subfault dimensions of 10.0 km along strike and 9.0 km along dip, and a uniform rupture velocity of 2.5 km/s. The subfault source time function is parameterized by six 3.5-s triangles shifted by 3.5 s, giving subfault durations of up to 24.5 s. The fault plane dip is 5.5° at 7.6-km depth, 31° at our adjusted hypocentral depth of 24.0 km, and 38° at 39.5-km deep (as shown in Figure 4a). The fault plane has a fixed strike (314°) and reference rake (70°) from the GCMT solution. The maximum water depth above the shallow end of the fault is 4.6 km. This will generate *pwP* ringing with periods less than 9 s. This model differs from that produced by Ye, Lay, et al. (2016) in doubling the length of the data window to 140 s, including *SH* data in the inversion, and using variable dip and water depth (there was no water layer in the earlier model).

The solution for this event has a concentrated large-slip patch of up to 6 m centered on the hypocenter, and a smaller region with 1.0- to 1.5-m slip up-dip from the hypocenter (Figures 15 and 16a). Slip does not extend to the seafloor. This model is quite similar to those obtained by the USGS-NEIC and Ye, Lay, et al. (2016). The moment-rate function (Figure 16c) has a relatively complex shape with two major pulses within 30 s and a weak tail of energy persisting to ~52 s. The centroid time is 16.8 s, and the seismic moment is 1.97 $\times 10^{20}$ Nm (M_w 7.46). Figure 16d shows a subset of waveform fits, with the match being good through about the first 50 s, but there is poor prediction of the subsequent complicated, large-amplitude coda, as is true for *SH* waveform fits (Figure S15). The strong coda arrivals near 60 s are not matched at all and cannot be attributed to *pwP* reverberations from shallow slip, even when we greatly reduce the along-dip rupture velocity to extend the source process time. While this event has the lowest *RMS_C/P* ratio (Figure 1) of the events considered here, some of the coda arrivals are large and have strong azimuthal variations (Figure S15), but these lack the stable ringing indicative of water multiples (Figures 3f and S6). Given the occurrence of late aftershocks with multiple focal mechanisms, we believe that the sustained motions after the direct *P* arrivals are best attributed to unresolved early aftershocks with diverse faulting mechanisms that produce temporally concentrated, azimuthally varying ground motions. Simple inspection by an analyst of the waveforms allows this inference to be made as soon as the ground motions are available, so the slightly elevated coda levels need not give false alarm of shallow slip enhancing tsunami amplitude. It is more challenging for a fully automatic real-time system to always recognize the distinction between impulsive coda and ringing coda, but a sufficiently trained neural net could probably do so.

4. Discussion About the Outlier Events

Analysis of outlier measurements is essential for confidence building in any warning system. Here we have selected the six prominent outliers in the *RMS_C/P* measurements shown in Figure 1 to evaluate why some high coda level events have low tsunamis, and for other events, whether their uncertain assigned classifications can be resolved. We sought to improve the slip models for all six large subduction zone thrust earthquakes by using quasi-2.5-D models for depth-varying fault dip and laterally varying bathymetry and by adjusting kinematic parameters to allow for the possibility of late shallow slip and associated strong *pwP* excitation, which can potentially increase the coda level for narrowband frequency reverberations. We find two categories of ruptures, schematically illustrated in Figure 17.

Two of the events clearly fall into the scenario involving rupture that includes slip at shallow depth on the megathrust with associated strong *pwP* ringing that enhances the high coda amplitudes (Figure 17a). This is the basic scenario invoked by Lay and Rhode (2019) and Lay et al. (2019). For the 30 July 1995 Chile and 17 November 2003 Aleutian events, late shallow slip of ~1 to 3 m efficiently generates associated *pwP* reverberations in the deep trench with 12- to 15-s period, accounting for observed very high relative P_{coda} levels for these two events (extending well beyond the time interval we invert). For these events, the shallow slip is patchy and separated from the primary slip patch at larger depth. Allowing for reduced along-dip rupture velocity and increased rupture duration allows the late slip to be captured, with the variable bathymetry enabling good prediction of the ensuing coda as late as 140 s after the *P* onset. There is modeling trade-off between

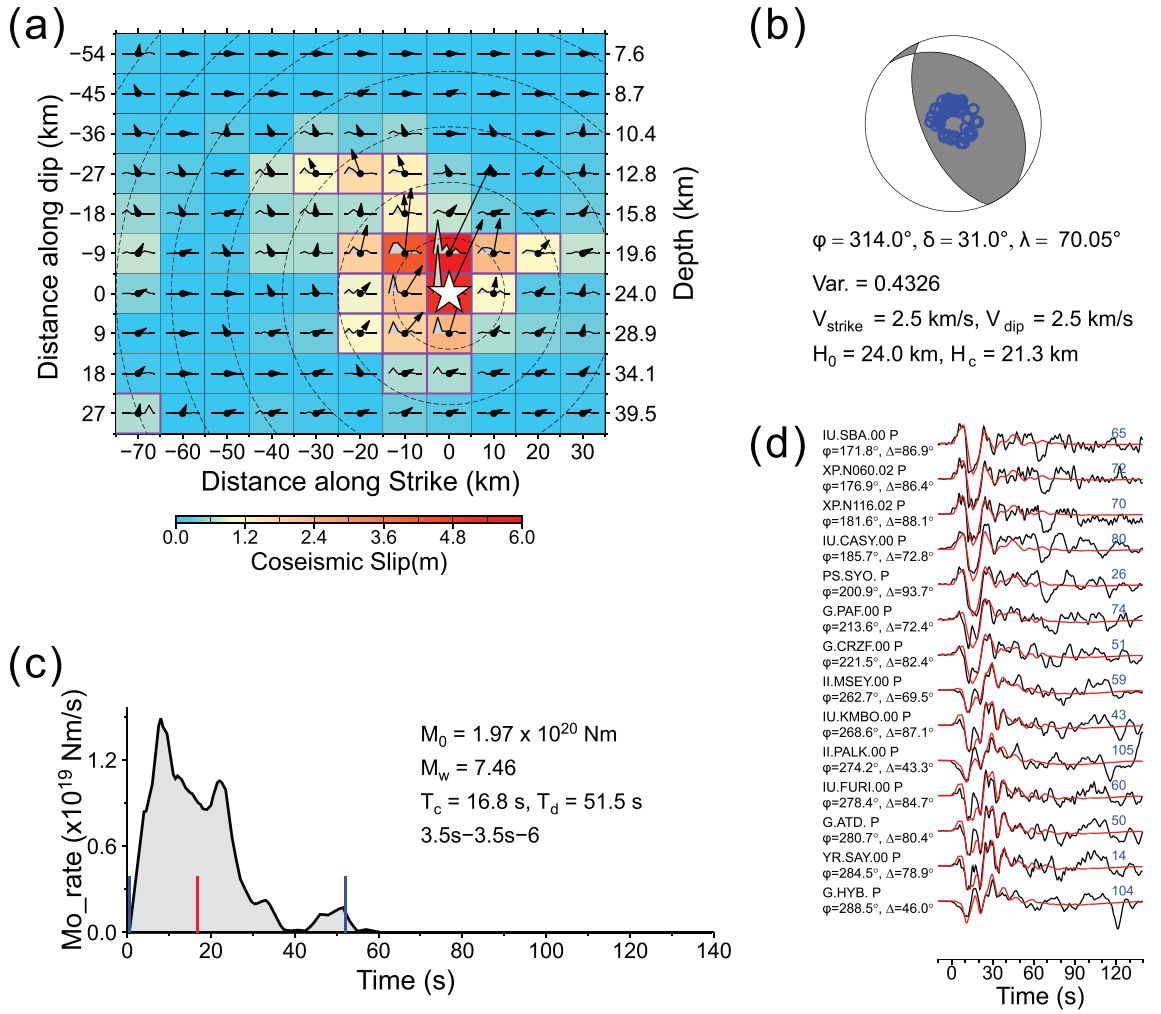

Figure 16. Finite-fault inversion for the 5 March 2002 M_w 7.5 Mindanao earthquake. The fault plane dip varies from 5.5° at 7.6 km depth to 38° at depth ~40 km. All panels follow the format of Figure 6. (a) The slip distribution with color-coded slip amplitude. (b) The average focal mechanism and *P* wave data distribution. (c) The moment-rate function. (d) A subset of comparisons of observed (black) and predicted (red) *P* waveforms. All waveform fits for this event are shown in Figure S15.

patchy shallow slip and ringing from associated *pwP* for our simplified modeling procedure. The inversions cannot resolve whether the rupture is truly continuous up to the shallow slip patches or whether these are dynamically triggered by the deeper slip driving conditionally stable regions to fail due to high strain rates or by triggering unstable patches within a predominantly stable sliding regime.

If we use the increased source durations for the moment-rate functions for our updated slip models to constrain the *P* and P_{coda} time intervals, we obtain for a rupture duration of 85 s for 1995 Chile *RMS_C/P* = 1.51 (versus 1.33 for a rupture duration of 62.5 s used in Figure 1) and for a rupture duration of 108 s for 2003 Aleutian *RMS_C/P* = 0.67 (versus 0.97 for a rupture duration of 39 s used in Figure 1). These values still correctly indicate occurrence of some shallow slip likely to have corresponding enhanced tsunami excitation. It is important to note that the shallow slip is small and not very tsunamigenic for these events; however, the modest tsunami observed for each case was probably enhanced or resulted entirely from the shallow slip. Small slip still gives only small tsunami excitation.

The second scenario involves the rupture of one or more discrete (triggered) early aftershocks in the time interval after the direct *P* wave motions from the main rupture, which increases *RMS_C/P* measurements (Figure 17b). The 7 October 2009 Vanuatu event has a compact large-slip region near the hypocenter, along with an up-dip small-slip region that contributes to raising the early coda level somewhat, but later discrete

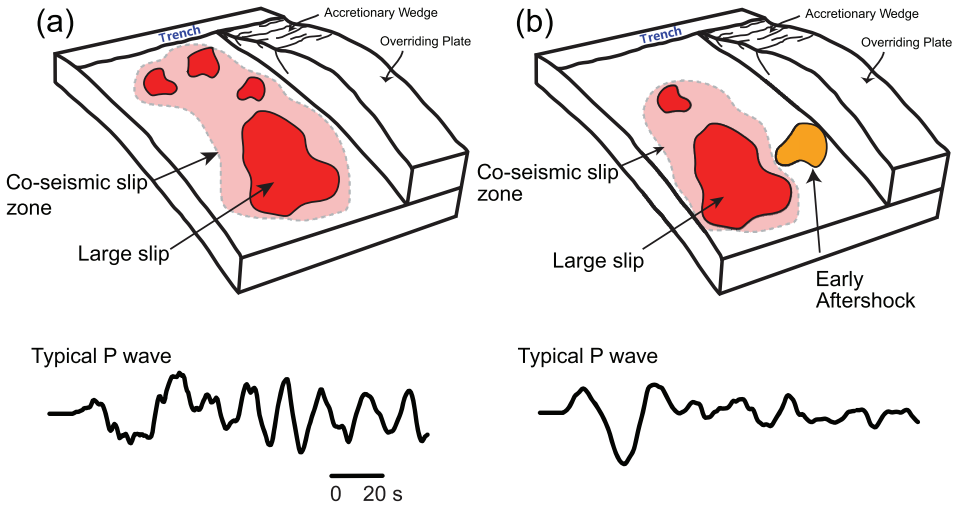

Figure 17. Schematic displays of two rupture situations inferred from our inversions that can result in high P_{coda}/P ratio without strong tsunami excitation. (a) Rupture with minor coseismic shallow slip patches near the deep-water trench that efficiently generates strong *pwP*. (b) Rupture lacking near trench shallow slip but with early interplate/intraplate aftershocks that can substantially raise the early coda level leading to high P_{coda}/P measures.

pulses from early aftershocks are mainly responsible for the high coda amplitudes. The 5 May 2015 Papua New Guinea event does not have shallow slip, but along strike triggering of adjacent thrust faulting in the form of early aftershocks (the first of which is imaged and has azimuthally varying relative arrival times that locate the source) is the explanation for the high P_{coda}/P measure. The 12 November 1996 Peru earthquake has most slip down-dip under the coastline, but minor up-dip slip accounts for the moderate, rapidly decaying early coda levels. Later arrivals that contribute to the moderately high P_{coda}/P ratio are not explained and may be due to either scattered *pwP* in the deeper trench to the southeast or early aftershocks. The 5 March 2002 Mindanao event has a relatively compact large-slip region near the hypocenter, with a small-slip region at shallower depth that does not reach the seafloor. The ground motions following the large-slip associated arrivals of this event are very complex and not modeled by rupture on the thrust plane at any depth; these are attributed to the early aftershocks with distinct focal mechanisms that cause azimuthally varying *P* waves relative to the main rupture.

For the 2009 Vanuatu, 2015 Papua New Guinea, 1996 Peru, and 2002 Mindanao events, with at most minor patchy slip regions up-dip of the main slip patch, the high coda levels are primarily attributed to triggered early interplate/intraplate aftershocks or scattered signals. If we use the durations of the coherent bursts of source-energy in Figure 3 to constrain the "effective" *P* and P_{coda} time intervals, we obtain for 55-s rupture duration for 2009 Vanuatu $RMS\_C/P = 0.89$ (versus 0.81 for a rupture duration of 40 s used in Figure 1) and 2015 Papua New Guinea $RMS\_C/P = 0.66$ for 90 s *P* interval (versus 0.82 for a rupture duration of 60 s used in Figure 1). The 2009 Vanuatu measure still correctly indicates the occurrence of some shallow slip, whereas the 2015 Papua New Guinea measure is now neutral as to whether shallow slip occurred. If we accept the slightly increased rupture duration of 70 s for the 1996 Peru event, found with or without shallow slip, $RMS\_C/P = 0.69$ (versus 0.75 for a rupture duration of 45 s used in Figure 1), slightly higher than for the 2015 event. It is hard to place reliable bounds on the effective *P* interval for the 2002 Mindanao event. From the perspective of applying the *RMS_C/P* procedure for rapid applications to tsunami warning, false alarm with respect to prospect of greater than normal (for a given M_W event) tsunami can be avoided by simply looking at the waveforms, by processing of spectrograms, or by designing a neural net to detect impulsive arrivals in the coda window (as for the 7 October 2009 Vanuatu event), with azimuthal variations in move-out times (as for the 5 May 2015 PNG event), and/or azimuthal variations in relative waveforms (as for the 12 November 1996 Peru and 5 March 2002 Mindanao events). The *RMS_C/P* measures above 0.8 in Figure 1 appear to provide reliable indicators of the presence of some shallow slip.

5. Conclusions

Rapid tsunami-warnings are issued based on rapid focal mechanism and seismic moment determinations, geodetic deformations, and nearby tsunami recordings. Improving rapid constraints on the rupture depths is desirable, particularly for large interplate thrust events. A recent approach involving measuring P_{coda}/P ratios from teleseismic recordings is designed to detect ringing coda generated by slip at shallow depth below deep water, which will enhance tsunami excitation relative to what might be expected for the given event size if rupture is confined to the typical central megathrust depth range. Many events with high P_{coda}/P measures are associated with finite-fault slip models that indicate at least some shallow rupture near the deep-water trench. However, four events with moderate to high P_{coda}/P measurements have inconsistent finite-fault models or no indication of shallow slip and two events with very high P_{coda}/P measurements have only small reported tsunami.

We reexamine the slip models of the six outliers and find that two different scenarios can account for the observed high coda levels. One scenario involves late shallow slip beneath deep water that generates water reverberations that enhance the coda. This holds for the 1995 Chile and 2003 Aleutian events. The shallow slip (~1–3 m) is patchy and separated from the deeper large-slip region. Routine finite-fault model parameterizations can miss this shallow slip due to ignoring the strong coda arrivals and/or kinematically constraining the rupture so that it cannot resolve any shallow slip. Even though the slip may be small, the efficiency of generating strong *pwP* is high, so high coda levels can be observed even if tsunami excitation is not high. For such events the coda measures are useful for inclusion in rapid tsunami warning that is primarily based on rapidly determined faulting geometry and seismic moment. The second scenario, inferred from analysis of the 1996 Peru, 2009 Vanuatu, 2015 PNG, and 2002 Mindanao events, involves relatively infrequent occurrence of scattered energy or early interplate or intraplate aftershocks within the time window soon after the main rupture process is complete, raising the coda level, but likely having little/no tsunami enhancement. This scenario needs to be addressed so it does not lead to false inference of enhanced tsunami excitation, and that can be done by analysts or waveform processing to distinguish impulsive coda arrivals from ringing *pwP* arrivals.

The coda attributes for these two scenarios are distinguishable and can guide the application of P_{coda}/P ratio measures in several ways. If the coda has apparent strong harmonic reverberations recorded at all azimuths, but especially at seaward azimuths, the event likely does have some shallow slip reaching to near the deep-water trench and rapid tsunami warning can reliably indicate the potential for enhanced tsunami for the given event size. If seismic wave distance profiles display coherent discrete ground motions without ringing motions, it is likely that an early aftershock occurred, leading to high P_{coda}/P measurement that is not a result of shallow slip, so no tsunami enhancement is likely. Differential time move-out relative to the first arrival can locate the secondary event in some cases. If an early aftershock has a faulting mechanism differing from the mainshock, azimuthally varying, incoherent discrete *P* waves will be observed. These results demonstrate that by paying attention to the data patterns to recognize contamination from rare early aftershocks, false alarms of enhanced tsunami can be avoided and even modestly elevated *RMS_C/P* measures can reliably contribute to rapid tsunami hazard assessment.

Acknowledgments
All of the broadband seismic waveforms used in this study were accessed from the Data Management Center of the Incorporated Research Institutions for Seismology (https://www.iris.edu/hq/). Centroid moment-tensor solutions were obtained from https://www.globalcmt.org/. Ocean bathymetry model ETOPO1 was obtained from NOAA (https://www.ngdc.noaa.gov/mgg/global/). The least-squared inversion software is adapted from the package of Kikuchi and Kanamori (http://wwweic.eri.u-tokyo.ac.jp/ETAL/KIKUCHI/), with an updated driver code provided in the supplement. We thank G. Hayes and an anonymous reviewer for their helpful comments on the manuscript. Z. Wu received support from Chengdu University of Technology and the National Natural Science Foundation of China (41704042). T. Lay's research on earthquakes is supported by U.S. National Science Foundation grant EAR1802364. L. Ye's earthquake studies are supported by National Natural Science Foundation of China (41874056).

References

Allen, T. I., & Hayes, G. P. (2017). Alternative rupture-scaling relationships for subduction interface and other offshore environments. *Bulletin of the Seismological Society of America*, *107*, 1240–1253. https://doi.org/10.1785/0120160255

Balakina, L. M., & Moskvina, A. G. (2009). Characterization of the seismogenic process in the Aleutian Island Arc: II. The large earthquakes of February 4, 1965, and November 17, 2003, in the Rat Island. *Physics of the Solid Earth*, *45*(3), 199–224. https://doi.org/10.1134/S1069351309030021

Beck, S., & Christensen, D. H. (1991). Rupture process of the February 4, 1995, Rat Islands earthquake. *Journal of Geophysical Research*, *96*, 2205–2221. https://doi.org/10.1029/90JB02092

Beck, S., & Ruff, J. (1985). The rupture process of the 1976 Mindanao earthquake. *Journal of Geophysical Research*, *90*, 6773–6782. https://doi.org/10.1029/JB090iB08p06773

Bilek, S. L., & Lay, T. (1999). Comparison of depth dependent fault zone properties in the Japan Trench and Middle America trench. *Pure and Applied Geophysics*, *154*, 433–456. https://doi.org/10.1007/s000240050238

Bilek, S. L., & Lay, T. (2018). Subduction zone megathrust earthquakes. *Geosphere*, *14*(4), 1468–1500. https://doi.org/10.1130/GES01608.1

Carlo, D. L., Lay, T., Ammon, C. J., & Zhang, J. (1999). Rupture process of the 1995 Antofagasta Subduction earthquake. *Pure and Applied Geophysics*, *154*(3-4), 677–708. https://doi.org/10.1007/s000240050248

Cleveland, K. M., Ammon, C. J., & Lay, T. (2014). Large earthquake processes in the northern Vanuatu subduction zone. *Journal of Geophysical Research - Solid Earth*, 8866–8883. https://doi.org/10.1002/2014JB011289

Cooper, P., & Taylor, B. (1989). Seismicity and focal mechanisms at the New Britain Trench related to deformation of the lithosphere. *Tectonophysics*, *164*, 25–40. https://doi.org/10.1016/0040-1951(89)90231-X

Delouis, B., Monfret, T., Dorbath, L., Rivera, L., Comte, D., Haessler, H., et al. (1997). The M_w = 8.0 Antofagasta (Northern Chile) Earthquake of 30 July 1995: A precursor to the end of the large 1877 gap. *Bulletin of the Seismological Society of America*, *87*, 427–445.

Geist, E. L., & Parsons, T. (2005). Triggering of tsunamigenic aftershocks from large strike-slip earthquakes: Analysis of the November 2000 New Ireland earthquake sequence. *Geochemistry, Geophysics, Geosystems*, *6*, Q10005. https://doi.org/10.1029/2005GC000935

Hayes, G. P. (2017). The finite, kinematic rupture properties of great-sized earthquakes since 1990. *Earth and Planetary Science Letters*, *468*, 94–100. https://doi.org/10.1016/j.epsl.2017.04.003

Hayes, G. P., Moore, G. L., Portner, D. E., Hearne, M., Flamme, H., Furtney, M., & Smoczyk, G. M. (2018). Slab2, a comprehensive subduction zone geometry model. *Science*, *363*, 58–61. https://doi.org/10.1126/science.aat4723

Heidarzadeh, M., Gusman, A. R., Harada, T., & Satake, K. (2015). Tsunamis from the 29 March and 5 May 2015 Papua New Guinea earthquake doublet (M_w 7.5) and tsunamigenic potential of the New Britain trench. *Geophysical Research Letters*, *42*, 5958–5965. https://doi.org/10.1002/2015GL064770

Ihmlé, P. F., & Madariaga, R. (1996). Monochromatic body waves excited by great subduction zone earthquakes. *Geophysical Research Letters*, *23*, 2999–3002. https://doi.org/10.1029/96GL02892

Ihmlé, P. F., & Ruegg, J. C. (1997). Source tomography by simulated annealing using broad-band surface waves and geodetic data: application to the M_w = 8.1 Chile 1995 event. *Geophysical Journal International*, *131*, 146–158. https://doi.org/10.1111/j.1365-246X.1997.tb00601.x

Kanamori, H. (1972). Mechanism of tsunami earthquakes. *Physics of the Earth and Planetary Interiors*, *6*, 346–359. https://doi.org/10.1016/0031-9201(72)90058-1

Kanamori, H. (2014). The diversity of large earthquakes and its implications for hazard mitigation. *Annual Review of Earth and Planetary Sciences*, *42*, 7–26. https://doi.org/10.1146/annurev-earth-060313-055034

Klotz, J., Angermann, D., Michel, G. W., Porth, R., Reigber, C., Reinking, J., et al. (1999). GPS-derived deformation of the Central Andes including the 1995 Antofagasta M_w = 8.0 earthquake. *Pure and Applied Geophysics*, *154*, 709–730. https://doi.org/10.1007/s000240050249

Lay, T. (2016). *Great earthquakes on plate boundaries*. Oxford Research Encyclopedia, Natural Hazard Science, 34 pp. https://doi.org/10.1093/acrefore/9780199389407.013.32

Lay, T. (2018). A review of the rupture characteristics of the 2011 Tohoku-oki M_W 9.1 earthquake. *Tectonophysics*, *733*, 4–36. https://doi.org/10.1016/j.tecto.2017.09.022

Lay, T., & Bilek, S. (2007). Anomalous earthquake ruptures at shallow depths on subduction zone megathrusts. In T. H. Dixon, & J. C. Moore (Eds.), *The Seismogenic Zone of Subduction Thrust Faults*, (pp. 476–511). New York: Columbia University Press.

Lay, T., & Kanamori, H. (1980). Earthquake doublets in the Solomon Islands. *Physics of the Earth and Planetary Interiors*, *21*, 283–304. https://doi.org/10.1016/0031-9201(80)90134-X

Lay, T., Kanamori, H., Ammon, C. J., Koper, K. D., Hutko, A. R., Ye, L., et al. (2012). Depth-varying rupture properties of subduction zone megathrust faults. *Journal of Geophysical Research - Solid Earth*, *117*, B04311. https://doi.org/10.1029/2011JB009133

Lay, T., Li, L., & Cheung, K. F. (2016). Modeling tsunami observations to evaluate a proposed late tsunami earthquake stage for the 16 September 2015 Illapel, Chile, M_W 8.3 earthquake. *Geophysical Research Letters*, *43*(15), 7902–7912. https://doi.org/10.1002/2016GL070002

Lay, T., Liu, C., & Kanamori, H. (2019). Enhancing tsunami warning using *P* wave coda. *Journal of Geophysical Research - Solid Earth*, *124*. https://doi.org/10.1029/2019JB018221

Lay, T., & Rhode, A. (2019). Evaluating the updip extent of large megathrust ruptures using P_{coda} levels. *Geophysical Research Letters*, *46*, 5198–5206. https://doi.org/10.1029/2019GL082774

Lay, T., Ye, L., Ammon, C. J., & Kanamori, H. (2017). Intraslab rupture triggering megathrust rupture coseismically in the 17 December 2016 Solomon Islands M_W 7.9 earthquake. *Geophysical Research Letters*, *44*, 1286–1292. https://dx.doi.org/10.1002/2017GL072539

Lay, T., Ye, L., Kanamori, H., Yamazaki, Y., Cheung, K. F., & Ammon, C. J. (2013). The Febraury 6, 2013 MW 8.0 Santa Cruz Islands earthquake and tsunami. *Tectonophysics*, *608*, 1109–1121. https://dx.doi.org/10.1016/j.tecto.2013.07.001

Lee, S.-J., Lin, T.-C., Feng, K.-F., & Liu, T.-Y. (2018). Composite megathrust rupture from deep interplate to trench of the 2016 Solomon Islands event. *Geophysical Research Letters*, *45*, 674–681. https://doi.org/10.1002/2017GL076347

Li, L., Lay, T., Cheung, K. F., & Ye, L. (2016). Joint modeling of teleseismic and tsunami observations to constrain the 16 September 2015 Illapel, Chile, MW 8.3 earthquake rupture process. *Geophysical Research Letters*, *43*, 4303–4312. https://dx.doi.org/10.1002/2016GL068674

Meier, M.-A., Ampuero, J. P., & Heaton, T. H. (2017). The hidden simplicity of subduction megathrust earthquakes. *Science*, *357*, 1277–1281 . https://doi.org/10.1126/science.aan5643

Park, S. C., & Mori, J. (2007). Are asperity patterns persistent? Implication from large earthquakes in Papua New Guinea. *Journal of Geophysical Research*, *112*, B03303. https://doi.org/10.1029/2006JB004481

Pritchard, M. E., Simons, M., Rosen, P. A., Hensley, S., & Webb, F. H. (2002). Co-seismic slip form the 1995 July 30 M_w = 8.1 Antofagasta, Chile, earthquake as constrained by InSAR and GPS observations. *Geophysical Journal International*, *150*, 362–376. https://doi.org/10.1046/j.1365-246X.2002.01661.x

Qian, Y., Wei, S., Wu, W., Zeng, H., Coudurier-Curveur, A., & Ni, S. (2019). Teleseismic waveform complexities caused by near trench structures and their impacts on earthquake source study: Application to the 2015 Illapel aftershocks (Central Chile). *Journal of Geophysical Research - Solid Earth*, *124*, 870–889. https://doi.org/10.1029/2018JB016143

Ruegg, J. C., Campos, J., Armijo, R., Barrientos, S., Briole, P., Thiele, R., et al. (1996). The M_w = 8.1 Antofagasta (North Chile) earthquake of July 30, 1995: First results from teleseismic and geodetic data. *Geophysical Research Letters*, *23*, 917–920. https://doi.org/10.1029/96GL01026

Salichon, J., Delouis, B., Lundgren, P., Giardini, D., Costantini, M., & Rosen, P. (2003). Joint inversion of broadband teleseismic and interferometric synthetic aperture radar (InSAR) data for the slip history of the M_w = 7.7, Nazca ridge (Peru) earthquake of 12 November 1996. *Journal of Geophysical Research*, *108*(B2), 2085. https://doi.org/10.1029/2001JB000913

Sladen, A., & Trevisan, J. (2018). Shallow megathrust earthquake ruptures betrayed by their outer-trench aftershocks signature. *Earth and Planetary Science Letters*, *483*, 105–113. https://doi.org/10.1016/j.epsl.2017.12.006

Spence, W., Mendoza, C., Engdahl, E. R., Choy, G. L., & Norabuena, E. (1999). Seismic subduction of the Nazca Ridge as shown by the 1996-97 Peru earthquakes. *Pure and Applied Geophysics*, *154*, 753–776. https://doi.org/10.1007/978-3-0348-8679-6_16

Stewart, G. S., & Cohn, S. N. (1979). The 1976 August 16, Mindanao, Philippine earthquake (M_w = 7.8)—Evidence for a subduction zone south of Mindanao. *Geophysical Journal International*, *57*, 51–65. https://doi.org/10.1111/j.1365-246X.1979.tb03771.x

Swenson, J. L., & Beck, S. L. (1999). Source characteristics of the 12 November 1996 M_w 7.7 Peru subduction zone earthquake. *Pure and Applied Geophysics*, *154*, 731–751. https://doi.org/10.1007/s000240050250

Vallée, M., & Douet, V. (2016). A new database of source time functions (STFs) extracted from the SCARDEC method. *Physics of the Earth and Planetary Interiors*, *257*, 149–157. https://doi.org/10.1016/j.pepi.2016.05.012

Wetzler, N., Lay, T., Brodsky, E. E., & Kanamori, H. (2017). Rupture-depth-varying seismicity patterns for major and great ($M_W \geq 7.0$) megathrust earthquakes. *Geophysical Research Letters*, *44*, 9663–9671. https://doi.org/10.1002/2017GL074573

Wetzler, N., Lay, T., Brodsky, E. E., & Kanamori, H. (2018). Systematic deficiency of aftershocks in areas of high coseismic slip for large subduction zone earthquakes. *Science Advances*, *4*. https://doi.org/10.1126/sciadv.aao3225

Wu, F. T., & Kanamori, H. (1973). Source mechanism of February 4, 1965, Rat Island earthquake. *Journal of Geophysical Research*, *78*, 6082–6092. https://doi.org/10.1029/JB078i026p06082

Wu, W., Ni, S., Zhan, Z., & Wei, S. (2018). A SEM-DSM three-dimensional hybrid method for modeling teleseismic waves with complicated source-side structures. *Geophysical Journal International*, *215*, 133–154. https://doi.org/10.1093/gji/ggy273

Yagi, Y. (2003). Source process of large and significant earthquakes in 2003. *Bulletin of the International Institute of Seismology and Earthquake Engineering*, 145–153.

Yagi, Y., & Fukahata, Y. (2011). Introduction of uncertainty of Green's function into waveform inversion for seismic source processes. *Geophysical Journal International*, *186*, 711–720. https://doi.org/10.1111/j.1365-246x.2011.05043.x

Yagi, Y., & Kikuchi, M. (2000). *Preliminary results of rupture process for November 16, 2000 New Ireland Region, Papua New Guinea earthquake*. Earthquake Res. Inst., Univ. of Tokyo, Tokyo. http://wwweic.eri.utokyo.ac.jp/yuji/PNG/index.html

Yamazaki, Y., Cheung, K. F., & Lay, T. (2018). A self-consistent fault slip model for the 2011 Tohoku earthquake and tsunami. *Journal of Geophysical Research - Solid Earth*, *123*, 1435–1458. https://doi.org/10.1002/2017JB014749

Ye, L., Kanamori, H., Avouac, J.-P., Li, L., Cheung, K. F., & Lay, T. (2016). The 16 April 2016, M_W 7.8 (M_S 7.5) Ecuador earthquake: A quasi-repeat of the 1942 M_S 7.5 earthquake and partial re-rupture of the 1906 M_S 8.6 Colombia-Ecuador earthquake. *Earth and Planetary Science Letters*, *454*, 248–258. https://doi.org/10.1016/j.epsl.2016.09.006

Ye, L., Lay, T., Kanamori, H., & Rivera, L. (2016). Rupture characteristics of major and great ($M_W \geq 7.0$) megathrust earthquakes from 1990 to 2015: 1. Source parameter scaling relationships. *Journal of Geophysical Research - Solid Earth*, *121*, 826–844. https://doi.org/10.1002/2015JB012426